The Astrophysical Journal, 874:97 (28pp), 2019 March 20 https://doi.org/10.3847/1538-4357/ab0b43

Chemical Abundances of Main-sequence, Turnoff, Subgiant, and Red Giant Stars from APOGEE Spectra. II. Atomic Diffusion in M67 Stars

Diogo Souto[1], C. Allende Prieto[2,3], Katia Cunha[1,4], Marc Pinsonneault[5], Verne V. Smith[6], R. Garcia-Dias[2,3], Jo Bovy[7,8], D. A. García-Hernández[2,3], Jon Holtzman[9], J. A. Johnson[5], Henrik Jönsson[10], Steve R. Majewski[11], Matthew Shetrone[12], Jennifer Sobeck[11], Olga Zamora[2,3], Kaike Pan[13], and Christian Nitschelm[14]
[1] Observatório Nacional, Rua General José Cristino, 77, 20921-400 São Cristóvão, Rio de Janeiro, RJ, Brazil; souto@on.br, diogodusouto@gmail.com
[2] Instituto de Astrofísica de Canarias, E-38205 La Laguna, Tenerife, Spain
[3] Departamento de Astrofísica, Universidad de La Laguna, E-38206 La Laguna, Tenerife, Spain
[4] Steward Observatory, University of Arizona, 933 North Cherry Avenue, Tucson, AZ 85721-0065, USA
[5] Department of Astronomy, The Ohio State University, Columbus, OH 43210, USA
[6] National Optical Astronomy Observatory, 950 North Cherry Avenue, Tucson, AZ 85719, USA
[7] Department of Astronomy and Astrophysics, University of Toronto, 50 St. George Street, Toronto, ON, M5S 3H4, Canada
[8] Dunlap Institute for Astronomy and Astrophysics, University of Toronto, ON M5S 3H4, Canada
[9] New Mexico State University, Las Cruces, NM 88003, USA
[10] Lund Observatory, Department of Astronomy and Theoretical Physics, Lund University, Box 43, SE-221 00 Lund, Sweden
[11] Department of Astronomy, University of Virginia, Charlottesville, VA 22904-4325, USA
[12] University of Texas at Austin, McDonald Observatory, USA
[13] Apache Point Observatory and New Mexico State University, P.O. Box 59, Sunspot, NM, 88349-0059, USA
[14] Centro de Astronomía (CITEVA), Universidad de Antofagasta, Avenida Angamos 601, Antofagasta 1270300, Chile
Received 2018 December 23; revised 2019 February 25; accepted 2019 February 26; published 2019 March 27

Abstract

Chemical abundances for 15 elements (C, N, O, Na, Mg, Al, Si, K, Ca, Ti, V, Cr, Mn, Fe, and Ni) are presented for 83 stellar members of the 4 Gyr old solar-metallicity open cluster M67. The sample contains stars spanning a wide range of evolutionary phases, from G dwarfs to red clump stars. The abundances were derived from near-IR (λ1.5–1.7 μm) high-resolution spectra ($R = 22{,}500$) from the SDSS-IV/Apache Point Observatory Galactic Evolution Experiment (APOGEE) survey. A 1D local thermodynamic equilibrium abundance analysis was carried out using the APOGEE synthetic spectral libraries, via χ^2 minimization of the synthetic and observed spectra with the qASPCAP code. We found significant abundance differences ($\sim$0.05–0.30 dex) between the M67 member stars as a function of the stellar mass (or position on the Hertzsprung–Russell diagram), where the abundance patterns exhibit a general depletion (in [X/H]) in stars at the main-sequence turnoff. The amount of the depletion is different for different elements. We find that atomic diffusion models provide, in general, good agreement with the abundance trends for most chemical species, supporting recent studies indicating that measurable atomic diffusion operates in M67 stars.

Key words: diffusion – infrared: stars – open clusters and associations: general – stars: abundances

1. Introduction

M67 (Messier 67; NGC 2682) is a well-studied open cluster, with an age and metallicity (4 Gyr and [Fe/H] = 0.0, respectively) similar to those of the Sun. A number of studies have determined the distance to the cluster (Yadav et al. 2008), its age (Yadav et al. 2008, Sarajedini et al. 2009), photometric colors and reddening (Taylor 2007, Sarajedini et al. 2009), as well as metallicity and individual chemical abundances (Cohen 1980, Foy & Proust 1981; Tautvaišiene et al. 2000; Pancino et al. 2010; Jacobson et al. 2011; Önehag et al. 2014; Liu et al. 2016; Bertelli Motta et al. 2018; Gao et al. 2018, and Souto et al. 2018). M67 is a "benchmark" Galactic open cluster and an excellent laboratory in which to study poorly understood processes in stellar astrophysics, such as abundance variations in open clusters.

The chemical composition of a star is inherited from the interstellar matter from which it forms; however, this composition changes over time due to internal stellar processes, such as gravitational settling or atomic diffusion. The approximation employed in the determination of abundances can also induce systematic errors in the inferred abundances, creating an apparent lack of homogeneity. Examples of such simplifications are the assumptions of hydrostatic equilibrium or local thermodynamic equilibrium (LTE).

Stellar clusters are useful astrophysical environments to study elemental abundance variations because of the reasonable assumption that stars in a cluster were born from the same molecular cloud at the same time. Several authors have studied the initial chemical homogeneity of open and globular clusters (De Silva et al. 2006, 2007, Reddy et al. 2012; Bovy 2016) and have, so far, not found any evidence of inhomogeneities in the initial stellar populations of open and globular clusters.

One well-known process that has been extensively observed in clusters is that as stars evolve into red giants, their surface carbon and nitrogen abundances are altered by the convectively driven first dredge-up of material from the stellar interior that has been exposed to H burning via the CN cycle (Bressan et al. 2012; Lagarde et al. 2012; Choi et al. 2016). This process does not, however, explain the lack of uniformity in the elemental abundances of main-sequence and turnoff stars found in metal-poor globular clusters (Korn et al. 2007, Lind et al. 2008; Nordlander et al. 2012). These variations are instead explained by atomic diffusion, a fundamental process predicted by theory (Michaud et al. 2015, references therein) and operating in all stars, which is often ignored in stellar evolution models and abundance studies. Atomic diffusion represents the physical process that involves the transport of material in the stellar atmosphere that is described by a diffusion equation, for

example, gravitational settling. Atomic diffusion has a physical basis, with diffusion coefficients predicted by theory; see Chapman (1917a, 1917b), Aller & Chapman (1960), Michaud et al. (1976), Vauclair et al. (1978), Michaud (1980), Vauclair & Vauclair (1982), and Michaud et al. (2004).

Diffusion in stars having a solar age and metallicity, as is the case for members of M67, has been theoretically investigated by Michaud et al. (2004), who analyzed 28 elements, finding that He, Li, Be, B, Mg, P, Ti, Fe, and Ni were those most affected by this mechanism. One of their conclusions was that atomic diffusion models can have a significant impact on the stellar ages derived from isochrones. More recently, theoretical calculations by Dotter et al. (2017) concluded that atomic diffusion also plays an important role in stars with a solar age and metallicity (not only metal-poor stars), and they found that the photospheric iron abundance in turnoff stars can be depleted by ∼0.12 dex compared to their initial surface abundance as a consequence of atomic diffusion processes. Dotter et al. (2017) noted that ignoring diffusion in models would cause an additional uncertainty of about 10% in the stellar ages derived from isochrones.

Evidence for the occurrence of diffusion in M67 stars has been found previously by Önehag et al. (2014), who studied a sample of 14 stars belonging to M67, including main-sequence stars (six), turnoff (three), and the early subgiant branch (five), using high-resolution optical spectra from FLAMES/UVES on the Very Large Telescope (VLT). Önehag et al. (2014) found abundance differences among the groups of 0.05–0.10 dex for Al, Ca, Cr, Mn, and Fe, with turnoff stars having lower abundances than subgiants. Blanco-Cuaresma et al. (2015) compiled a sample of 42 stars in M67 (28 main sequence and 14 red giants) using spectra from the ESPaDOnS twin spectropolarimeter atop Pic du Midi (NARVAL), High Accuracy Radial velocity Planet Searcher (HARPS), and Ultraviolet and Visual Echelle Spectrograph (UVES). The authors observed that the abundances of Na, Mg, and Si show variations of up to 0.10–0.20 dex between dwarf and giant stars in the cluster.

Souto et al. (2018, Paper I) studied a small sample of eight M67 stellar members spanning a range of evolutionary phases, including G dwarfs (two), G-turnoff stars (two), G subgiants (two), and red clump K giants (two) using high-resolution spectra from the Apache Point Observatory Galactic Evolution Experiment (APOGEE; Majewski et al. 2017). They found abundance variations in 14 elements across the Hertzsprung–Russell (H-R) diagram, confirming that most chemical species display changes in the range of 0.05–0.20 dex (Fe, Na, Mg, Al, Si, Ca, and Mn), with the lower abundances observed in turnoff stars, with $M \sim 1.2 M_{\odot}$. Souto et al. (2018) also showed that the abundance variations found in M67 stars compare very well with theoretical models of atomic diffusion for stars having solar age and metallicity. Also using APOGEE spectra, Bertran de Lis et al. (2016) found significantly more dispersion in [O/Fe] for M67 stars than for other clusters with similar metallicity but younger ages, such as NGC 6819 or NGC 2158. Bovy (2016) and Price-Jones & Bovy (2018) found strong constraints on the chemical homogeneity in M67 red giant stars from APOGEE. The authors showed that M67 red giants are homogeneous based only on their stellar spectra, without the need of modeling the stellar atmosphere. The uniformity within the red giant stars may indicate that changes in the stellar abundances across different evolutionary phases in the H-R diagram for M67 might be related to physical processes operating within these stars.

The works of Bertelli Motta et al. (2018) and Gao et al. (2018) have confirmed, using independent data, that atomic diffusion operates in M67 stars. Both works used high-resolution optical spectra. Bertelli Motta et al. (2018) used UVES/FLAMES ($R \sim 20{,}000$–$32{,}000$) observations from the *Gaia*/ESO survey (Gilmore et al. 2012, Randich et al. 2013), reporting abundances of 11 elements in 15 stars from the main sequence, turnoff, and red giant branch (RGB). Bertelli Motta et al. (2018), using APOGEE data, find abundance variations of up to 0.20–0.30 dex for elements like Al, Mn, and Ni, where non-LTE effects are unlikely to explain the observed trends. Gao et al. (2018) use spectra from the GALAH survey (De Silva et al. 2015), with a resolving power of $R \sim 28{,}000$, to report abundances for seven elements in 66 stars from the turnoff, subgiant, red giant, and red clump phases. Gao et al. (2018) conclude that deviations from non-LTE can explain some of the observed abundance trends as a function of the evolutionary stage, in particular for oxygen and sodium. However, for Al and Si, non-LTE does not explain the remaining trend, which the authors argue might be a consequence of diffusion processes in M67.

This work provides a complementary verification of the atomic diffusion mechanisms acting in M67 stars as reported by Souto et al. (2018). We use APOGEE results obtained with the qASPCAP[15] pipeline using a much larger stellar sample; qASPCAP is a simple IDL script that substitutes the entire ASPCAP (APOGEE Stellar Parameters and Chemical Abundances Pipeline, García Pérez et al. 2016) for boutique work.

APOGEE targeted M67 as one of its calibration clusters, observing about 100 stellar members from the lower main sequence, the turnoff, the subgiant branch, and the RGB. The M67 APOGEE sample is well suited both to probe the limits on chemical homogeneity in the cluster members and to search for signatures of atomic diffusion in the chemical abundances of a number of elements. APOGEE spectra are used here to derive detailed chemical abundances of 15 elements: C, N, O, Na, Mg, Al, Si, K, Ca, Ti, V, Cr, Mn, Fe, and Ni.

The paper is structured as follows: in Section 2 we describe the adopted sample, in Section 3 we report on the atmospheric parameters and the methodology employed to derive the individual abundances, in Section 4 we analyze the abundance trends, and in Section 5 we suggest possible explanations for them. In Section 6 we discuss the obtained results, summarizing in Section 7.

2. APOGEE Data on M67

The APOGEE spectrographs are cryogenic multifiber near-infrared instruments covering the *H* band between $\lambda 1.51$ μm and $\lambda 1.69$ μm, obtaining high-resolution ($R = \lambda/\Delta\lambda \sim 22{,}500$) spectra for 300 objects at a time (Gunn et al. 2006; Wilson et al. 2010). The spectrographs are currently mounted in both hemispheres on 2.5 m telescopes at APO (Apache Point Observatory, New Mexico, USA) and at LCO (Las Campanas Observatory, La Serena, Chile). The M67 stellar spectra analyzed in this work were all obtained at APO and reduced with the APOGEE pipeline, described in Nidever et al. (2015).

[15] github.com/callendeprieto/

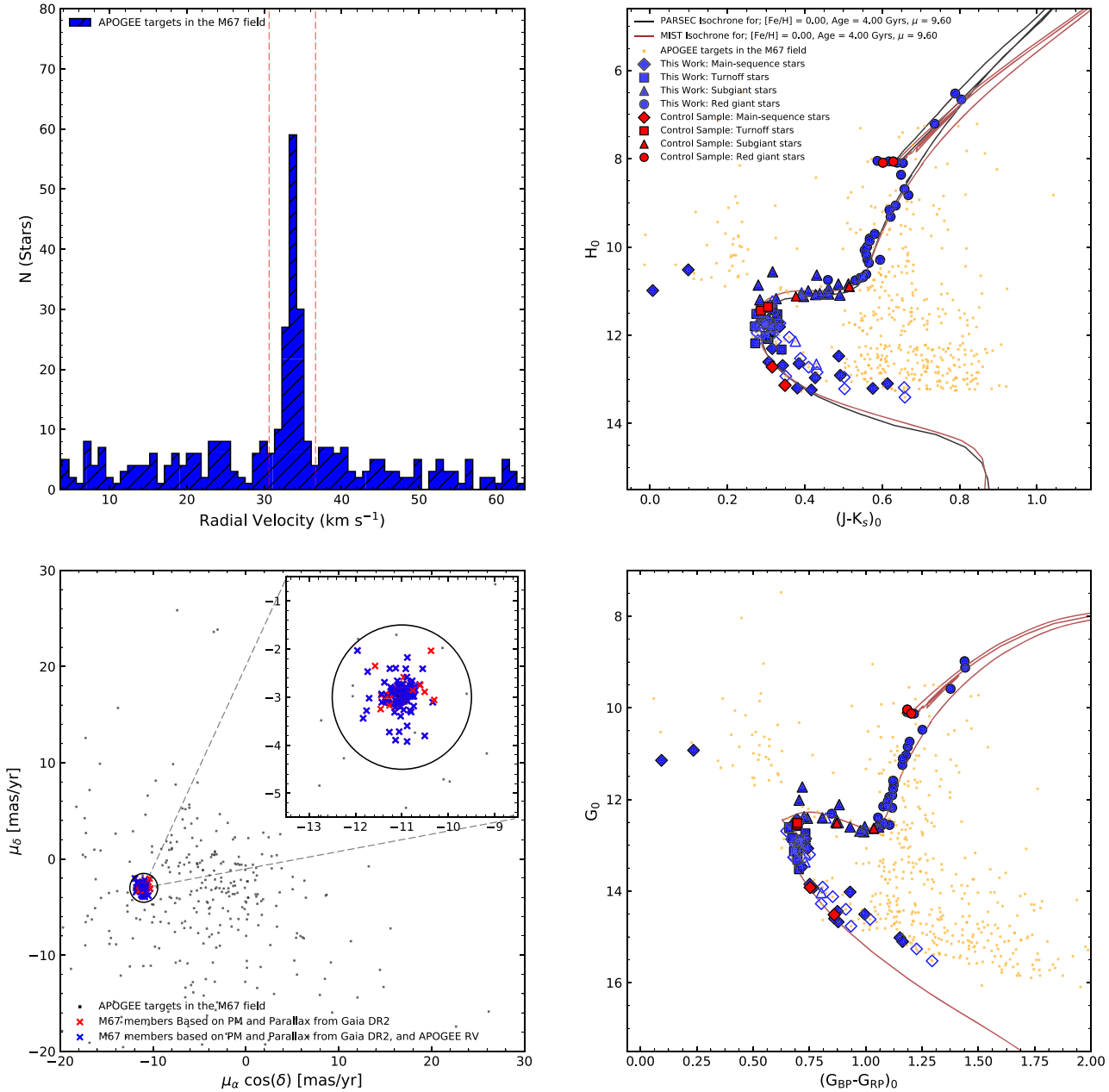

Figure 1. Top left panel: radial velocity distribution obtained from ASPCAP for all of the targets observed in the APOGEE M67 field. Bottom left panel: vector-point diagram with the adopted stellar proper motions. Top right panel: $(J-K_s)_0$ vs. H_0 diagram showing the sample of this work. We represent the main-sequence stars as blue diamonds, blue squares are the turnoff stars, the blue triangles are the subgiants, and the blue circles represent the red giant stars. We also include the stellar sample of Souto et al. (2018) using the same symbol notation for the stellar classes, but colored as red. The 2MASS color–magnitude diagram of the APOGEE targets in the M67 field is shown as orange dots. Two isochrones for an age of 4 Gyr, $(m\text{–}M)_0 = 9.60$, and [Fe/H] = 0.00 from PARSEC (black line) and the MESA Isochrones and Stellar Tracks (MIST; brown line) are also shown. We left as open symbols the stars with S/N < 100. Bottom right panel: same as top right panel, expect the color–magnitude diagram using *Gaia* DR2 data for $(G_{BP}\text{–}G_{RP})_0$ vs. G_0.

APOGEE is part of the SDSS-III and SDSS-IV projects (Eisenstein et al. 2011, Blanton et al. 2017), and M67 is one of the calibration clusters for the ASPCAP pipeline (Mészáros et al. 2013; Zasowski et al. 2013; Holtzman et al. 2015; García Pérez et al. 2016). APOGEE has observed a dedicated field in the direction of M67 (location ID 4162), obtaining spectra for 563 targets. The stars had multiple visits, generally more than three, to reach the required signal-to-noise ratio (S/N) of the combined spectra (higher than ∼100 per half a resolution element); this was achieved for stars brighter than $H \leqslant 11$.

To verify membership of the observed stars in the M67 APOGEE field, we adopt two approaches, one using membership studies from the literature and another using distances and proper motions from *Gaia* DR2 (Gaia Collaboration et al. 2018). We initially used the radial velocities (RV) measured by the APOGEE pipeline available in the 14th SDSS data release (DR14, Abolfathi et al. 2018), following the proper motion and RV membership criteria of Yadav et al. (2008) and Geller et al. (2015) as guidelines. Yadav et al. (2008) determined proper motions for 2462 stars using the Wide-Field-Imager from the MPG/ESO 2.2 m telescope at La Silla, Chile, with a field of view of 34 × 33 arcmin^2. The authors reported 434 stars having membership probabilities ⩾90%. Using the same data, Bellini et al. (2010) derived the cluster average proper motion to be μ_α

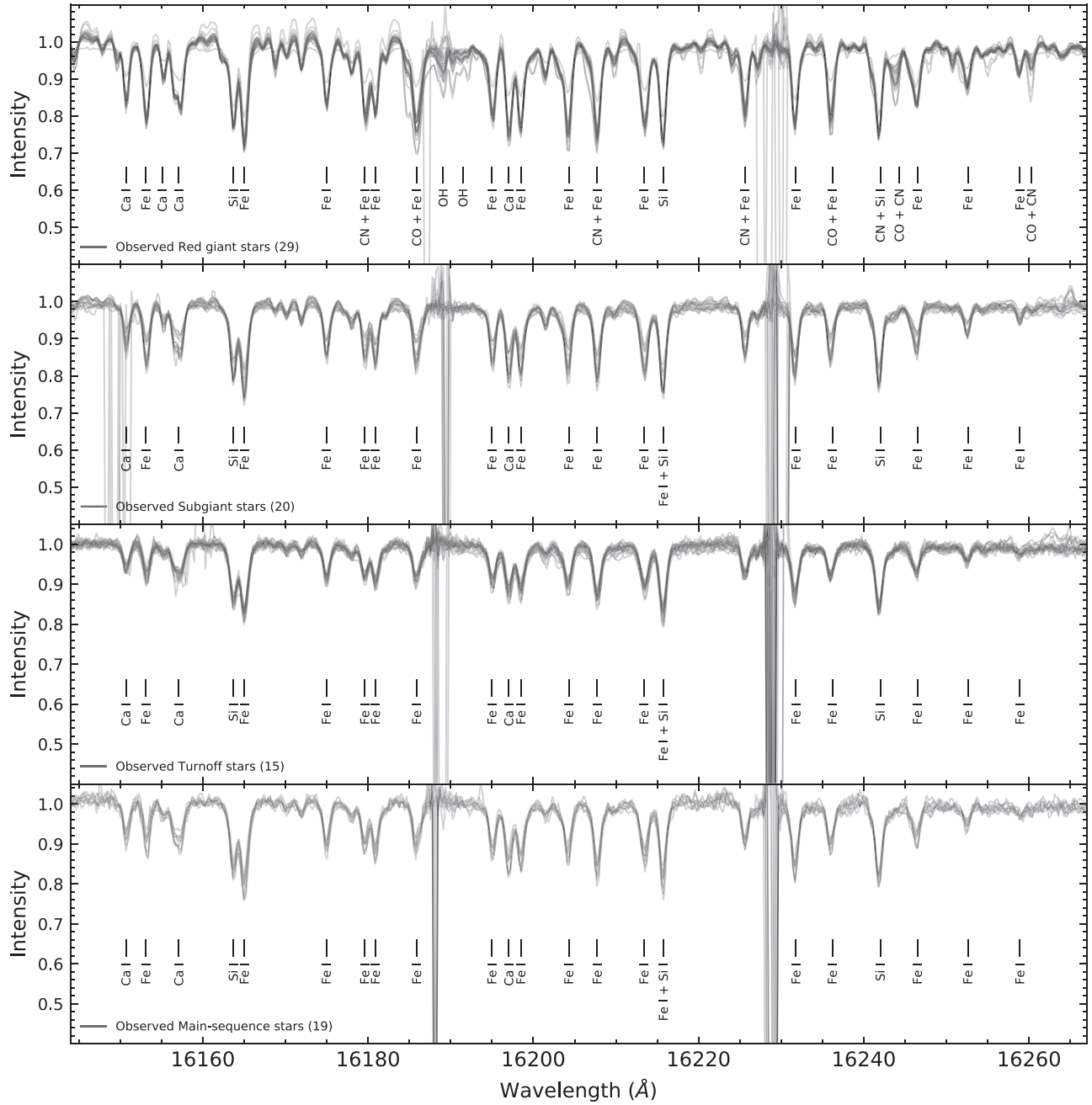

Figure 2. Portion of the APOGEE observed spectra for the stellar sample. From top to bottom, we shown the spectra of red giant, subgiant, turnoff, and main-sequence stars.

$\cos(\delta) = -9.6 \pm 1.1$ mas yr^{-1} and $\mu_\delta = -3.7 \pm 0.8$ mas yr^{-1}. The radial velocity survey by Geller et al. (2015) used spectra obtained from various sources, including a total of 1278 stars in the vicinity of M67. Geller et al. (2015) reported 590 stars having membership probabilities $\geqslant$90%, where the mean radial velocity of the sample is 33.64 km s^{-1}, with high internal precision (0.03 km s^{-1}).

Based on this information, an initial membership cut was performed, selecting from the targets observed in the M67 APOGEE field (563 stars), those within the radial velocity range 30.64–36.64 km s^{-1}. Figure 1 (top left panel) shows a histogram of the RV distribution of all the stars in the field. The peak of the RV distribution compares well with the mean radial velocity for the cluster reported by Geller et al. (2015), with 140 stars falling within the RV limit (red dashed lines). We then performed a cross-match between the stars within the limit in radial velocity and those stars reported by Yadav et al. (2008) and Geller et al. (2015) having membership probabilities $\geqslant$90%. A total of 119 stars satisfied these criteria.

We then adopted *Gaia* DR2 (Gaia Collaboration et al. 2018) proper motions with distances from Bailer-Jones et al. (2018) to refine the sample. From those 140 stars within the RV limits, we find 109 within the ranges in distance and proper motion for M67. We accepted stars with distances in the range 796.2–992.0 pc, which corresponds to a distance modulus of 9.56–9.88, as reported in the literature for the cluster (Yadav et al. 2008, Yakut et al. 2009). We then adopted the mean proper motions observed for the stars within the adopted

Table 1
Stellar Properties

2Mass ID	RV (km s^{-1})	σ(RV) σ(km s^{-1})	PM (R.A.) ($\mu_\alpha \cos(\delta)$)	PM (R.A.) σ	PM (Decl.) (μ_δ)	PM (Decl.) σ	Dist BJ18 parsec	Dist (σ) parsec	S/N	Prob G15	Prob Y08	Prob Z93	Prob G89	Prob S77	J	H	K_s
Red Giants																	
2M08492491+1144057	35.09	1.51	−11.06	0.07	−2.87	0.05	829.45	28.15	460	98	99	99	99	2	10.296	9.831	9.708
2M08503613+1143180	34.29	0.11	−11.06	0.07	−2.74	0.06	873.89	24.21	138	72	100	93	97	94	11.131	10.644	10.552
2M08504964+1135089	34.92	0.07	−10.96	0.08	−2.96	0.06	832.42	28.06	344	98	99	94	99	95	9.410	8.848	8.722
2M08511269+1152423	34.34	0.07	−10.95	0.06	−2.98	0.04	818.41	12.56	1445	98	99	99	96	95	8.650	8.122	7.976
2M08511704+1150464	33.58	0.06	−11.16	0.07	−3.32	0.05	829.68	28.19	371	98	99	77	97	95	9.284	8.712	8.606
2M08511897+1158110	34.01	0.10	−11.08	0.06	−3.09	0.04	847.08	23.29	384	98	100	94	98	51	10.587	10.095	10.012
2M08512156+1146061	34.87	0.06	−11.10	0.08	−2.66	0.05	834.37	31.65	314	97	98	91	99	95	9.602	9.085	8.947
2M08512618+1153520	34.16	0.04	−11.00	0.07	−2.88	0.05	842.43	14.79	982	97	97	77	99	95	8.619	8.113	7.960
2M08512898+1150330	33.46	0.04	−11.14	0.08	−3.22	0.05	812.29	18.46	481	98	100	94	98	95	8.566	8.072	7.958
2M08512990+1147168	36.28	0.01	−11.27	0.09	−3.73	0.05	795.23	34.60	884	98	99	0	96	96	7.314	6.681	6.489
2M08513577+1153347	34.05	0.11	−11.06	0.06	−2.93	0.04	801.49	20.07	205	98	93	99	72	95	10.522	10.023	9.941
2M08513938+1151456	33.98	0.11	−11.10	0.07	−3.12	0.04	834.61	26.61	469	98	100	95	99	93	10.383	9.889	9.795
2M08514234+1150076	34.27	0.05	−11.02	0.07	−2.80	0.05	805.95	23.64	271	98	0	99	99	96	9.829	9.339	9.187
2M08514388+1156425	32.94	0.05	−11.18	0.11	−3.16	0.07	844.60	22.86	505	95	100	99	98	91	8.618	8.114	7.996
2M08514507+1147459	32.97	0.04	−11.05	0.07	−3.03	0.04	839.67	26.03	281	97	99	2	92	92	9.684	9.183	9.045
2M08514883+1156511	34.35	0.05	−10.96	0.08	−3.26	0.05	858.95	35.02	135	97	99	99	99	94	11.256	10.779	10.705
2M08515611+1150147	34.68	0.04	−11.13	0.08	−3.89	0.05	843.67	28.77	133	98	99	99	98	95	11.197	10.726	10.634
2M08515952+1155049	34.39	0.05	−11.00	0.09	−3.10	0.06	868.56	21.45	543	98	99	88	91	90	8.597	8.084	7.959
2M08521097+1131491	33.82	0.03	−11.06	0.06	−2.76	0.04	822.72	23.87	672	98	100	92	98	96	8.921	8.388	8.252
2M08521656+1119380	33.82	0.03	−11.05	0.07	−2.88	0.05	808.61	30.73	1073	97	100	71	38	94	7.875	7.233	7.119
2M08521856+1144263	33.65	0.06	−11.13	0.07	−3.14	0.05	818.62	13.28	504	96	100	95	98	94	8.572	8.087	7.923
2M08522636+1141277	33.41	0.10	−10.77	0.08	−2.99	0.05	784.76	28.62	196	97	99	99	99	0	10.845	10.314	10.263

Table 1
(Continued)

2Mass ID	RV (km s^{-1})	σ(RV) σ(km s^{-1})	PM (R.A.) ($\mu_\alpha \cos(\delta)$)	PM (R.A.) σ	PM (Decl.) (μ_δ)	PM (Decl.) σ	Dist BJ18 parsec	Dist (σ) parsec	S/N	Prob G15	Prob Y08	Prob Z93	Prob G89	Prob S77	J	H	K_s
2M08525625+1148539	32.84	0.07	−11.02	0.08	−3.10	0.05	870.52	33.96	195	97	99	99	99	77	10.839	10.315	10.224
2M08534672+1123307	33.04	0.07	−11.24	0.08	−2.79	0.05	864.38	32.99	370	nan	nan	nan	nan	nan	10.225	9.730	9.624
2M08493465+1151256	33.98	0.08	−10.98	0.06	−2.92	0.04	904.59	nan	1369	98	98	99	91	96	7.203	6.546	6.394
2M08505816+1152223	34.03	0.11	−11.13	0.08	−2.86	0.05	884.25	34.01	287	98	99	99	96	91	11.197	10.707	10.626
2M08510723+1153019	32.99	30.95	−10.92	0.07	−2.41	0.05	903.98	21.87	604	11	100	99	97	71	11.175	10.771	10.695
2M08510839+1147121	33.52	0.18	−10.91	0.08	−2.93	0.06	888.63	28.60	171	98	98	99	99	93	10.691	10.195	10.112
2M08522003+1127362	33.94	0.05	−11.22	0.07	−2.91	0.04	893.78	28.66	260	98	99	93	91	89	10.839	10.383	10.253
Subgiants																	
2M08504994+1149127	33.83	0.10	−10.83	0.07	−3.27	0.05	809.79	28.26	110	98	100	94	97	93	11.372	10.960	10.890
2M08510325+1145473	35.11	0.21	−11.07	0.08	−2.91	0.06	829.30	27.10	103	61	96	54	99	95	11.491	11.220	11.187
2M08511564+1150561	34.01	0.03	−10.73	0.07	−2.78	0.05	785.07	21.58	209	86	100	99	98	94	11.485	11.094	11.013
2M08511670+1145293	35.48	0.21	−11.26	0.13	−2.41	0.09	843.16	51.73	140	nan	nan	nan	nan	nan	11.021	10.662	10.570
2M08512122+1145526	33.49	0.69	−11.74	0.09	−2.47	0.06	852.74	38.64	110	98	98	95	99	95	11.135	10.888	10.835
2M08512879+1151599	33.59	0.13	−10.91	0.07	−3.04	0.05	840.04	26.19	116	98	97	99	99	92	11.433	11.104	11.024
2M08512935+1145275	33.14	0.06	−10.74	0.07	−2.98	0.04	837.93	27.28	135	98	98	99	99	95	11.287	10.864	10.754
2M08513540+1157564	33.39	0.05	−11.10	0.07	−3.01	0.04	848.14	24.64	238	98	96	96	99	95	11.447	11.143	11.030
2M08513862+1220141	33.74	0.12	−10.95	0.08	−3.00	0.05	858.14	32.96	251	98	25	99	97	93	11.298	10.866	10.791
2M08514401+1146245	33.11	0.13	−11.10	0.07	−2.89	0.05	870.91	29.12	116	95	99	99	98	95	11.438	11.110	11.027
2M08514474+1146460	33.12	0.06	−11.06	0.07	−3.12	0.04	798.50	23.63	351	98	100	99	98	92	11.357	10.918	10.822
2M08514994+1149311	33.33	0.13	−11.35	0.07	−3.10	0.04	858.19	27.21	205	98	99	99	99	0	11.494	11.196	11.148
2M08515335+1148208	34.28	0.04	−11.44	0.07	−2.94	0.04	817.06	26.68	189	98	99	7.	nan	99	90	11.625	11.390
2M08521134+1145380	33.05	0.04	−10.98	0.07	−2.99	0.04	858.43	27.32	113	98	98	99	37	0	11.452	11.082	10.993

Table 1
(Continued)

2Mass ID	RV (km s^{-1})	σ(RV) σ(km s^{-1})	PM (R.A.) ($\mu_\alpha \cos(\delta)$)	PM (R.A.) σ	PM (Decl.) (μ_δ)	PM (Decl.) σ	Dist BJ18 parsec	Dist (σ) parsec	S/N	Prob G15	Prob Y08	Prob Z93	Prob G89	Prob S77	J	H	K_s
2M08503667 +1148553	35.36	0.22	−11.43	0.06	−3.11	0.04	899.99	30.68	162	97	99	99	98	96	11.930	11.628	11.578
2M08505569 +1152146	34.08	0.09	−11.01	0.18	−2.84	0.13	930.54	57.06	425	97	99	99	95	95	10.852	10.586	10.515
2M08510106 +1150108	32.90	0.14	−10.79	0.09	−2.93	0.06	899.78	30.39	117	97	100	93	98	87	11.380	11.018	10.951
2M08510951 +1141449	32.36	0.08	−10.33	0.07	−3.11	0.06	897.57	30.12	113	97	100	99	47	0	11.445	11.102	10.997
2M08511877 +1151186	34.07	0.10	−10.98	0.07	−2.74	0.05	883.67	33.72	333	98	0.0	99	99	95	11.502	11.089	11.020
2M08515567 +1217573	33.52	0.05	−10.99	0.08	−2.86	0.06	935.73	37.02	226	96	100	99	98	96	11.516	11.115	11.005
Turnoff																	
2M08503392 +1146272	33.78	0.14	−10.97	0.08	−3.05	0.06	869.53	32.54	241	98	99	99	99	96	11.824	11.596	11.517
2M08504079 +1147462	34.59	0.06	−10.89	0.07	−3.08	0.05	847.32	28.41	170	98	99	86	98	93	11.793	11.540	11.498
2M08505177 +1200247	33.72	0.25	−11.22	0.05	−2.85	0.05	867.93	21.00	146	75	99	16	94	95	12.377	12.106	12.051
2M08505702 +1159158	33.96	0.22	−11.06	0.05	−3.72	0.03	840.73	21.18	178	98	100	99	98	94	12.003	11.726	11.673
2M08505762 +1155147	33.07	0.24	−10.71	0.04	−2.85	0.03	870.75	17.25	148	98	100	94	98	93	12.294	12.038	11.973
2M08505903 +1148576	33.67	0.44	−10.97	0.05	−2.73	0.03	867.89	21.19	118	94	100	99	99	96	12.386	12.206	12.094
2M08505973 +1139524	33.21	0.19	−10.62	0.07	−2.74	0.05	831.18	28.29	104	98	100	99	99	96	12.025	11.735	11.703
2M08510969 +1159096	33.98	7.27	−10.79	0.04	−2.93	0.03	857.36	14.81	154	98	99	99	72	94	12.658	12.348	12.298
2M08511576 +1152587	35.82	0.08	−11.96	0.07	−2.03	0.05	844.46	29.65	162	98	99	99	99	64	11.728	11.453	11.391
2M08512240 +1151291	33.44	0.16	−10.94	0.05	−2.96	0.04	853.50	20.51	132	98	99	94	84	79	12.195	11.952	11.862
2M08513710 +1154599	34.85	0.05	−10.85	0.04	−2.95	0.03	858.09	19.44	127	96	99	99	0	0	12.096	11.819	11.763
2M08513806 +1201243	32.14	0.12	−11.03	0.06	−3.40	0.04	839.80	28.69	144	98	99	99	99	69	11.844	11.551	11.495
2M08514122 +1154290	33.61	0.21	−11.15	0.07	−3.06	0.05	820.44	25.67	213	83	98	99	81	94	11.703	11.466	11.397
2M08514475 +1145012	34.89	0.20	−10.87	0.04	−2.81	0.03	855.48	18.41	136	98	97	99	99	95	12.288	12.039	11.969
2M08520741 +1150221	34.19	0.16	−11.12	0.04	−2.95	0.03	864.00	18.90	202	98	99	99	77	83	12.097	11.823	11.806

Table 1
(Continued)

2Mass ID	RV (km s^{-1})	σ(RV) σ(km s^{-1})	PM (R.A.) ($\mu_\alpha \cos(\delta)$)	PM (R.A.) σ	PM (Decl.) (μ_δ)	PM (Decl.) σ	Dist BJ18 parsec	Dist (σ) parsec	S/N	Prob G15	Prob Y08	Prob Z93	Prob G89	Prob S77	J	H	K_s
Main Sequence																	
2M08502805 +1154505	34.95	0.20	−10.55	0.04	−2.41	0.03	860.00	19.59	122	98	100	99	99	93	12.968	12.665	12.563
2M08511229 +1154230	35.13	0.26	−10.81	0.05	−2.87	0.04	850.83	21.65	118	98	97	99	98	91	12.986	12.708	12.623
2M08512314 +1154049	33.62	0.33	−10.83	0.05	−2.76	0.03	846.83	20.20	119	98	98	99	93	94	13.017	12.741	12.681
2M08512604 +1149555	32.89	0.30	−11.76	0.06	−3.28	0.04	853.19	25.88	137	98	97	99	98	92	13.344	12.987	12.897
2M08512996 +1151090	34.82	0.23	−11.07	0.05	−3.08	0.03	855.38	22.12	192	98	99	89	99	93	12.926	12.630	12.599
2M08513119 +1153179	34.17	0.30	−10.82	0.04	−2.98	0.03	858.47	19.64	156	98	99	99	97	95	12.603	12.327	12.267
2M08513701 +1136516	33.18	0.67	−10.80	0.06	−3.31	0.04	848.99	24.24	100	98	100	92	98	94	13.341	12.932	12.829
2M08514189 +1149376	35.88	0.28	−11.02	0.06	−2.92	0.04	862.75	25.07	112	98	98	99	98	95	13.626	13.262	13.189
2M08514742 +1147096	31.44	6.03	−11.11	0.05	−3.09	0.03	840.28	19.47	113	98	99	95	99	96	12.880	12.496	12.372
2M08521649 +1147382	33.91	0.27	−11.01	0.07	−2.74	0.04	814.76	28.03	120	98	99	99	99	77	13.558	13.221	13.157
2M08505439 +1156290	33.73	0.11	−10.74	0.07	−3.19	0.05	919.56	34.20	270	98	98	99	99	95	11.706	11.435	11.372
2M08510076 +1153115	34.05	0.28	−10.76	0.06	−2.93	0.05	914.22	28.97	119	96	100	96	97	93	13.474	13.157	13.105
2M08511176 +1150018	33.53	0.29	−11.02	0.08	−3.20	0.05	899.09	29.78	127	3	100	96	98	92	13.665	13.120	13.031
2M08512080 +1145024	33.77	0.11	−10.51	0.06	−3.81	0.04	889.07	28.43	109	nan	89	97	95	99	11.928	11.679	11.603
2M08512742 +1153265	34.28	0.18	−10.87	0.06	−3.09	0.04	948.69	34.44	273	95	96	99	98	95	11.667	11.382	11.342
2M08512788 +1155409	36.06	0.18	−11.13	0.04	−2.40	0.03	893.36	18.68	129	98	100	99	99	95	12.168	11.831	11.813
2M08513012 +1143498	33.53	0.23	−11.11	0.09	−3.09	0.06	887.79	38.35	102	98	1	99	99	99	12.011	11.761	11.694
2M08513455 +1149068	33.53	0.41	−11.05	0.08	−3.20	0.05	887.52	27.47	104	98	91	96	99	95	13.717	13.229	13.121
2M08521868 +1143246	32.73	0.18	−10.97	0.07	−2.86	0.04	877.95	32.18	143	98	99	88	99	75	11.590	11.352	11.259
2M08512643 +1143506	33.45	0.26	−11.37	0.11	−2.69	0.08	835.57	38.90	121	98	100	96	99	95	11.020	11.011	10.993
2M08513259 +1148520	33.74	0.27	−11.30	0.08	−3.11	0.05	791.70	28.99	146	96	98	99	87	0	10.645	10.541	10.526

Table 1
(Continued)

2Mass ID	RV (km s^{-1})	σ(RV) σ(km s^{-1})	PM (R.A.) ($\mu_\alpha \cos(\delta)$)	PM (R.A.) σ	PM (Decl.) (μ_δ)	PM (Decl.) σ	Dist BJ18 parsec	Dist (σ) parsec	S/N	Prob G15	Prob Y08	Prob Z93	Prob G89	Prob S77	J	H	K_s
Excluded sample due to low S/N (<100) Subgiant																	
2M08503438 +1139566	33.77	0.21	−10.79	0.07	−2.94	0.05	850.43	27.79	99	98	99	91	98	96	11.513	11.244	11.177
2M08504198 +1136525	34.46	0.10	−11.12	0.07	−3.10	0.05	852.64	27.51	91	99	99	99	99	0	11.410	11.062	10.998
2M08510811 +1201065	33.83	0.23	−11.70	0.04	−3.02	0.03	875.47	20.06	99	98	96	99	99	95	12.469	12.159	12.073
2M08511826 +1150196	34.28	4.21	−10.89	0.06	−2.59	0.04	863.61	27.89	86	98	99	94	98	96	13.042	12.680	12.592
2M08520356 +1141238	34.15	0.07	−10.82	0.07	−2.76	0.04	852.79	27.94	99	98	99	99	99	89	11.634	11.365	11.306
Main Sequence																	
2M08502833 +1142097	33.75	0.39	−10.85	0.07	−2.83	0.05	832.76	25.30	64	98	97	99	98	88	11.899	11.654	11.587
2M08503788 +1252295	32.37	0.30	−11.83	0.07	−3.44	0.05	801.51	25.81	99	nan	nan	nan	nan	nan	13.662	13.239	13.139
2M08505334 +1143399	32.72	0.33	−10.89	0.05	−3.92	0.04	841.16	21.35	89	98	100	99	98	94	13.058	12.746	12.628
2M08505923 +1146129	31.98	1.78	−10.90	0.05	−2.84	0.03	810.49	18.26	55	98	100	99	98	96	12.271	11.998	11.934
2M08512386 +1138521	34.61	0.35	−11.04	0.06	−2.81	0.05	849.79	23.97	89	98	99	99	80	95	13.313	12.952	12.942
2M08513215 +1136126	34.34	0.41	−11.22	0.04	−2.83	0.03	869.31	17.26	52	94	96	99	99	89	12.207	11.965	11.910
2M08513444 +1137574	34.02	0.12	−10.78	0.04	−2.66	0.03	829.37	17.97	58	98	97	99	67	1	12.102	11.864	11.778
2M08514375 +1145148	32.40	0.19	−11.22	0.06	−2.94	0.04	848.12	24.69	55	98	97	99	99	95	12.027	11.805	11.729
2M08514465 +1141510	32.95	0.27	−11.33	0.04	−2.95	0.03	860.46	17.58	67	97	99	99	98	95	12.120	11.887	11.802
2M08515290 +1146358	34.00	0.53	−11.09	0.09	−2.78	0.05	865.42	23.43	97	98	94	99	99	94	13.961	13.429	13.282
2M08521664 +1142300	32.23	3.99	−10.94	0.05	−2.95	0.03	805.89	17.43	70	98	96	99	97	92	12.403	12.144	12.104
2M08504511 +1136023	31.15	13.33	−10.81	0.08	−2.70	0.07	842.68	17.27	76	97	99	99	98	71	13.800	13.210	13.123
2M08510131 +1141587	32.07	10.61	−11.04	0.04	−2.81	0.03	879.70	20.72	80	96	100	99	98	95	12.420	12.167	12.075
2M08510156 +1147501	32.93	0.23	−10.89	0.05	−3.60	0.04	876.51	23.19	57	98	100	93	98	96	12.371	12.067	11.991
2M08511229 +1146212	31.51	0.28	−10.93	0.05	−3.04	0.04	919.79	20.28	73	98	99	93	91	91	12.060	11.751	11.704

Table 1
(Continued)

2Mass ID	RV (km s^{-1})	σ(RV) σ(km s^{-1})	PM (R.A.) ($\mu_\alpha \cos(\delta)$)	PM (R.A.) σ	PM (Decl.) (μ_δ)	PM (Decl.) σ	Dist BJ18 parsec	Dist (σ) parsec	S/N	Prob G15	Prob Y08	Prob Z93	Prob G89	Prob S77	J	H	K_s
2M08511810+1142547	33.88	0.11	−10.96	0.05	−2.89	0.04	923.46	25.50	97	99	99	0	84	94	12.186	11.879	11.844
2M08512033+1145523	33.66	0.29	−10.89	0.06	−2.96	0.04	876.62	24.68	76	98	84	99	99	94	12.061	11.822	11.767
2M08512176+1144050	32.79	0.46	−11.28	0.05	−3.12	0.04	881.45	24.05	60	96	99	96	97	96	12.907	12.547	12.498
2M08512467+1143061	32.01	0.32	−10.88	0.07	−2.18	0.05	926.54	36.75	82	98	99	99	83	94	13.258	12.863	12.806
2M08513424+1145535	34.19	0.46	−10.83	0.07	−2.81	0.05	941.80	35.23	77	98	4	99	99	95	13.374	12.976	12.852

Note. Proper motions and distances from *Gaia* DR2.

distance limits, where $\mu_\alpha \cos(\delta) = -11.02 \pm 0.07$ mas yr^{-1} and $\mu_\delta = -2.97 \pm 0.05$ mas yr^{-1}. We consider as members the stars within ± 1 mas yr^{-1} from those mean values. Figure 1 bottom left panel displays the proper motions for the sample.

We removed from the sample two hot stars (2M08512643 + 1143506 and 2M08513259+1148520) likely to be blue stragglers. In the final sample, we will only retain the stars with *Gaia* DR2 data, confirming the membership criteria based on distances and proper motions. We searched for binary stars in our sample looking for RV variations in the multiple spectral visits, with none found. Also, we verify the lack of binary stars in comparing our sample (44 stars in common) with the recent work of El-Badry et al. (2018), where the authors detected more than 3000 binary stars in the APOGEE data. To ensure the quality of the observed spectra, we keep only those having S/N $\geqslant$ 100, resulting in a sample of 83 stars spanning the H-R diagram, from the main sequence to the red clump. The threshold in S/N is intended to minimize the uncertainties in the parameters derived. As we are searching for small abundance variations across the H-R diagram, we assemble the best possible sample. We will include the results reported by Souto et al. (2018) as a control or comparison sample. In Table 1 we present our sample, with the adopted radial velocity and S/N (from DR14), proper motions and distances (Gaia Collaboration et al. 2018), membership probabilities computed by Geller et al. (2015) and the adopted magnitudes, V (Zacharias et al. 2015), and 2MASS infrared magnitudes J, H, and K_S (Skrutskie et al. 2006). At the bottom of the table, we also provide data for those stars with S/N $<$ 100.

In the top right and bottom right panels of Figure 1, we display the color–magnitude diagram (CMD) $(J-K_S)_0$ versus H_0 and $(G_{BP}–G_{RP})_0$ versus G_0 for the studied sample using 2MASS and *Gaia* DR2 photometry, respectively. We show all 563 stars observed in the M67 field by the APOGEE survey with orange dots. Our sample stars are shown as filled symbols, and the ones with S/N $<$ 100 as empty symbols. We note that four early G and K dwarfs show a small offset compared to the adopted isochrones presented in the CMD diagrams of Figure 1, which could indicate nonmembership; however, we opt to use these stars because their RVs, proper motions, and distances suggest membership. The same symbol notation adopted by Souto et al. (2018) was used in this work, where diamonds correspond to main sequence, squares to turnoff stars, triangles for subgiants, and the circles represent the red giant stars, in blue for this work and red for Souto et al. (2018).

In Figure 2, we display a portion of the observed APOGEE spectra between 16150 and 16260 Å for the sample stars. From top to bottom, we plot the spectra of the red giant stars followed by the subgiant, turnoff, and main-sequence stars. The individual stellar spectra are very similar within a class, with rms differences at any given wavelength of about $\sigma = 0.01$. The largest star-to-star differences in Figure 2 are associated with CO, CN, and OH lines in the red giant spectra, suggestive of the changes produced by H burning in the stellar interior brought to the surface by the first dredge-up, as discussed in Section 5. Fe I and Ca I show the largest spread among G-type stars.

3. Stellar Parameters and Chemical Abundances

In this paper, we need to determine abundances in different classes of stars (dwarfs to red giants) homogeneously and precisely. One important factor in such analysis is the determination of the stellar parameters. It is known that the raw $\log g$ values derived using the ASPCAP pipeline contain systematic offsets for dwarfs (being systematically low) as well as red giant stars (being systematically high).

Figure 3 shows the effective temperature and surface gravity diagrams for our sample. The left panel shows the DR14 raw ASPCAP $T_{\rm eff}$ and $\log g$ results. It is clear that the $\log g$ values derived by ASPCAP do not match the isochrones from Bressan et al. (2012) and Choi et al. (2016) (presented in the figure). Using such $\log g$ values in the analysis would introduce systematic uncertainties in the derived abundances. In the next section, we discuss the determination of the $\log g$'s and adopted $T_{\rm eff}$ values in this study.

3.1. Effective Temperatures

We adopted the effective temperatures derived from ASPCAP DR14. We used the purely spectroscopic raw $T_{\rm eff}$ values from ASPCAP (given in the FPARAM array in DR14). For comparison, we also determined photometric temperatures by adopting the calibration of González-Hernández & Bonifacio (2009) and using five different colors, $B-V$, $V-J$, $V-H$, $V-K_s$, and $J-K_s$, with an adopted cluster reddening of $E(B-V) = 0.041$ mag (Sarajedini et al. 2009) and a metallicity of [Fe/H] = 0.00. González-Hernández & Bonifacio (2009) provide photometric calibrations for red giant and dwarf stars; we adopted the coefficients for giants for those stars with $\log g < 4.00$ dex and for dwarfs for those stars with higher gravities. Good agreement between the photometric and the adopted raw ASPCAP $T_{\rm eff}$ scales is obtained, where $\langle \delta(T_{\rm eff}({\rm ASPCAP} - {\rm GHB}) \rangle = -25 \pm 106$ K. The effective temperatures obtained from the ASPCAP pipeline have an internal precision of ± 50 K (Holtzman et al. 2015, García Pérez et al. 2016).

3.2. Surface Gravities

We determined surface gravities from the fundamental Equation (1), where the adopted $T_{\rm eff}$ values are from the raw ASPCAP DR14 values, with stellar masses and bolometric magnitudes obtained from interpolation in the MIST isochrones (Choi et al. 2016; [Fe/H] = 0.00; age = 4.00 Gyr; $E(B-V) = 0.041$; distance modulus (μ) = 9.60). The adopted solar values are $\log g_\odot = 4.438$ dex, $T_{\rm eff,\odot} = 5772$ K, and $M_{\rm bol,\odot} = 4.75$, following the IAU recommendations in Prša et al. (2016):

$$\log g = \log_{10} g_\odot + \log_{10}\left(\frac{M_\star}{M_\odot}\right) + 4\log_{10}\left(\frac{T_\star}{T_\odot}\right) + 0.4(M_{\rm bol,\star} - M_{\rm bol,\odot}). \quad (1)$$

We adopted the surface gravities derived from Equation (1) in the abundance analysis in this study. The uncertainties in the determined surface gravities are similar to the ones reported in Souto et al. (2018), where $\sigma = \pm 0.10$ dex. The comparison between the derived $\log g$ values in this work with those from ASPCAP confirms the $\log g$ offset, where we obtain $\langle \delta(\log g$ (Physical-ASPCAP)$\rangle = -0.18 \pm 0.16$ dex for red giants, -0.16 ± 0.11 dex for subgiants, -0.19 ± 0.07 dex for turnoff, and 0.17 ± 0.13 dex for main-sequence stars.

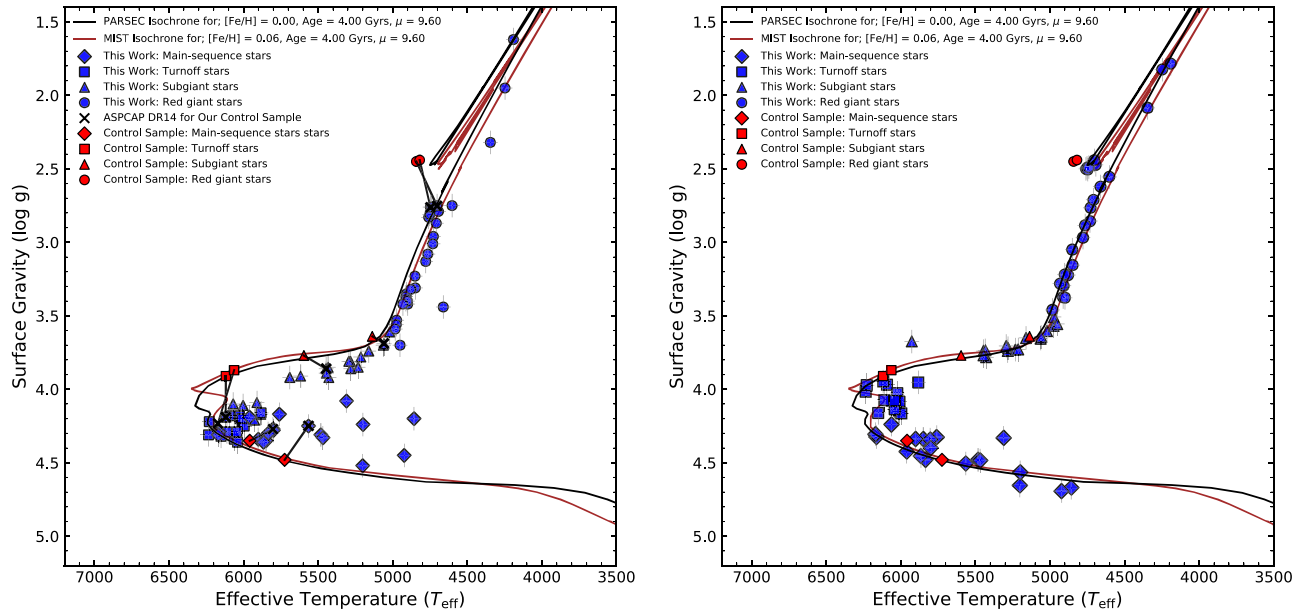

Figure 3. Left panel: $T_{\rm eff}$–log g diagram showing the APOGEE DR14 raw ASPCAP results for the M67 members. Note the mismatch with the isochrones due to systematic uncertainties in the log g values derived by ASPCAP. Right panel: $T_{\rm eff}$–log g diagram showing the stellar parameters adopted in this study. The $T_{\rm eff}$ values are the same raw values from ASPCAP DR14 shown in the left panel, but the surface gravities were derived from fundamental relations. The symbol notation is the same as in Figure 1.

Figure 3 (right panel) shows the $T_{\rm eff}$–log g values adopted in this study. The effective temperatures for the studied stars are well spread out in the H-R diagram, with effective temperatures ranging between 4200 and 6250 K. The surface gravity values for the studied stars span a range in log g = 1.78–4.71.

3.3. Individual Abundance Analysis

In this work, we derive individual abundances for 15 elements: C, N, O, Na, Mg, Al, Si, K, Ca, Ti, V, Cr, Mn, Fe, and Ni. Individual abundances were determined with the qASPCAP code. The qASPCAP code basically corresponds to the ASPCAP pipeline, but for custom work, providing flexibility to change the analysis parameters. The methodology in the analysis is the same as adopted in ASPCAP, and the optimization is based on the FERRE code.

The procedure for determining individual abundances and microturbulent velocities with qASPCAP is similar to the one in ASPCAP. The ASPCAP pipeline (described in detail in García Pérez et al. 2016) uses a grid of synthetic spectra (Zamora et al. 2015) computed with the turbospectrum code (Alvarez & Plez 1998, Plez 2012) using KURUCZ model atmospheres (Castelli & Kurucz 2004, Mészáros et al. 2012) and the APOGEE DR14 line list, which is an updated version of the one published in Shetrone et al. (2015). The stellar parameters and chemical abundances are obtained by χ^2 minimization with the FERRE code (Allende Prieto et al. 2006) controlled by an IDL wrapper (the qASPCAP in this work).

In a first phase, seven parameters are determined through a 7D optimization ($T_{\rm eff}$, log g, [M/H], [C/Fe], [N/Fe], [α/Fe], and ξ) using the entire wavelength range of the APOGEE spectra. During the second phase, individual abundances are obtained by repeating the fitting in predetermined windows that are sensitive to elemental abundances using the set of atmospheric parameters determined in the previous phase. It is possible to determine individual abundances for more than 26 elements from the APOGEE spectra; see Holtzman et al. (2018), Hasselquist et al. (2016, for Nd), and Cunha et al. (2017, for Ce). In this work, we adopt the same molecular and atomic lines as Souto et al. (2018) to derive individual abundances (see also Smith et al. 2013 and Souto et al. 2016). Even though Souto et al. (2018) reported Na and Cr abundances for main-sequence and turnoff stars, we opt in this work to not present these abundances (for these stellar classes) as the comparisons between the observed and synthesis were not satisfactory due to the weakness of the Na I and Cr I lines.

All M67 targets studied here have similar $v \sin(i)$, in the range $0 \leqslant v \sin(i) \leqslant 7\,{\rm km\,s^{-1}}$. In fact, the threshold to detect the star's $v \sin(i)$ from APOGEE spectra is 7–8 km s^{-1}. The effect of macroturbulence on the line profiles is similar to that of stellar rotation, and, as an approximation, qASPCAP treats rotation and macroturbulence as a single Gaussian profile.

The stellar parameters adopted in this work are shown in Table 2, with individual abundances presented in Table 3. The uncertainties in the derived abundances adopted in this work are the same as the ones reported in Table 4 of Souto et al. (2018). We note that, using ASPCAP calibrated abundances, the average $\langle \delta A({\rm El}) \rangle$ between the results derived in this work minus ASPCAP is smaller by 0.10 dex for all elements.

4. Results

The individual abundances reported in this work display an elevated scatter (standard deviation of the mean), in particular for nitrogen (∼0.14 dex), aluminum (∼0.16 dex), and the alpha elements (∼0.15 dex). The potassium abundances are the ones showing the smallest scatter, with $\sigma = 0.07$ dex. Such significant scatter in M67 stars was also noticed by Bertran de Lis et al. (2016) studying [O/Fe] in M67 stars with APOGEE and comparing it with the spread in other clusters.

Table 2
Stellar Parameters

2Mass ID	$T_{\rm eff}$ (K) ASPCAP raw	$T_{\rm eff}$ (K) ASPCAP calib	$T_{\rm eff}$ (K) GB09	log g (cm s^{-2}) ASPCAP raw	log g (cm s^{-2}) ASPCAP calib	log g (cm s^{-2}) Physical	Mass ($M_{\odot}$) Mass isochrone	ξ (km s^{-1}) ASPCAP raw
Red Giants								
2M08492491+1144057	4848.2	4893.5	4899.0	3.31	3.17	3.15	1.32	1.14
2M08503613+1143180	4973.6	5023.9	5019.9	3.53	3.41	3.51	1.31	1.24
2M08504964+1135089	4727.8	4774.7	4710.9	2.96	2.80	2.77	1.33	1.33
2M08511269+1152423	4758.1	4805.4	4702.4	2.83	2.49	2.50	1.33	1.45
2M08511704+1150464	4707.8	4757.9	4764.2	2.87	2.71	2.71	1.33	1.42
2M08511897+1158110	4907.5	4956.5	4909.9	3.35	3.22	3.30	1.32	1.11
2M08512156+1146061	4731.2	4776.9	4748.2	3.01	2.85	2.86	1.33	1.35
2M08512618+1153520	4750.6	4798.5	4714.2	2.81	2.48	2.49	1.33	1.40
2M08512898+1150330	4693.6	4741.1	4691.2	2.79	2.46	2.47	1.34	1.43
2M08512990+1147168	4247.5	4302.4	4274.0	1.95	1.68	1.82	1.34	1.47
2M08513577+1153347	4911.4	4959.5	4882.8	3.37	3.24	3.29	1.32	1.19
2M08513938+1151456	4878.3	4927.4	4871.1	3.32	3.20	3.22	1.32	1.20
2M08514234+1150076	4778.7	4825.8	4803.5	3.13	2.99	2.97	1.33	1.27
2M08514388+1156425	4747.5	4795.8	4711.9	2.76	2.44	2.50	1.33	1.64
2M08514507+1147459	4765.1	4812.5	4799.6	3.08	2.93	2.88	1.33	1.35
2M08514883+1156511	4976.0	5027.4	5028.8	3.56	3.44	3.57	1.31	1.25
2M08515611+1150147	4950.8	4994.9	4927.9	3.70	3.56	3.56	1.31	0.92
2M08515952+1155049	4740.0	4789.0	4708.4	2.76	2.45	2.49	1.33	1.51
2M08521097+1131491	4602.3	4649.1	4633.6	2.75	2.56	2.55	1.33	1.38
2M08521656+1119380	4345.3	4394.8	4406.8	2.32	2.09	2.08	1.35	1.39
2M08521856+1144263	4702.7	4750.1	4737.3	2.75	2.44	2.44	1.35	1.49
2M08522636+1141277	4912.3	4962.6	4957.1	3.39	3.26	3.37	1.31	1.30
2M08525625+1148539	4899.5	4944.1	4874.3	3.42	3.28	3.38	1.31	1.29
2M08534672+1123307	4850.6	4899.3	4880.3	3.23	3.11	3.05	1.32	1.10
2M08493465+1151256	4190.5	−9999.0	4347.6	1.62	−9999.	1.78	1.34	0.53
2M08505816+1152223	4983.5	5030.7	5021.5	3.59	3.46	3.46	1.31	1.05
2M08510723+1153019	4661.0	−9999.0	5335.0	3.44	−9999.	2.62	1.33	0.72
2M08510839+1147121	4901.4	4948.9	4995.6	3.40	3.27	3.22	1.32	1.25
2M08522003+1127362	4932.4	4980.3	4973.2	3.42	3.29	3.28	1.32	1.20
Subgiants								
2M08504994+1149127	5160.9	5213.0	5196.8	3.74	3.62	3.65	1.30	0.96
2M08510325+1145473	5884.4	5928.1	5932.2	4.17	−9999.	3.84	1.30	0.77
2M08511564+1150561	5282.5	5331.6	5271.0	3.81	−9999.	3.74	1.30	1.04
2M08511670+1145293	5280.6	5335.8	5312.0	3.86	−9999.	3.72	1.24	0.87
2M08512122+1145526	5926.6	5971.3	6019.4	4.21	−9999.	3.67	1.31	0.75
2M08512879+1151599	5617.4	5673.6	5624.3	3.91	−9999.	3.82	1.29	0.78
2M08512935+1145275	5019.9	5069.7	5061.7	3.61	3.49	3.60	1.31	1.16
2M08513540+1157564	5446.4	5497.9	5484.9	3.86	−9999.	3.74	1.29	0.65
2M08513862+1220141	5062.5	5112.0	4995.6	3.70	3.58	3.66	1.30	0.94
2M08514401+1146245	5432.7	5483.9	5507.6	3.85	−9999.	3.73	1.30	0.89
2M08514474+1146460	5058.6	5109.2	5065.6	3.69	3.57	3.64	1.30	0.97
2M08514994+1149311	6003.3	6048.3	5887.6	4.11	−9999.	3.85	1.28	0.83
2M08515335+1148208	6069.2	6114.7	5991.7	4.10	−9999.	3.89	1.27	1.06
2M08521134+1145380	5293.2	5343.2	5326.3	3.81	−9999.	3.71	1.30	0.92
2M08503667+1148553	5689.4	5746.5	5874.4	3.92	−9999.	3.82	1.29	0.68
2M08505569+1152146	5910.2	5954.9	5943.0	4.09	−9999.	3.85	1.28	0.67
2M08510106+1150108	5428.1	5480.6	5540.4	3.92	−9999.	3.78	1.29	0.82
2M08510951+1141449	5445.3	5492.3	5462.4	3.89	−9999.	3.77	1.29	0.84
2M08511877+1151186	5231.5	5277.7	5326.9	3.85	−9999.	3.73	1.30	0.81
2M08515567+1217573	5213.3	5264.6	5215.4	3.78	3.66	3.73	1.30	0.91
Turnoff								
2M08503392+1146272	6235.1	6279.1	6165.5	4.31	−9999.	4.02	1.25	0.73
2M08504079+1147462	6228.8	6274.8	6156.4	4.22	−9999.	3.97	1.25	0.72
2M08505177+1200247	6009.0	6053.3	6042.0	4.22	−9999.	4.15	1.21	0.62
2M08505702+1159158	6024.5	6069.9	6040.1	4.20	−9999.	4.03	1.27	0.55
2M08505762+1155147	6151.3	6196.3	6044.2	4.32	−9999.	4.16	1.21	0.64
2M08505903+1148576	5996.1	−9999.0	6090.9	4.25	−9999.	4.17	1.21	0.66
2M08505973+1139524	6061.8	6107.0	5968.9	4.34	−9999.	4.08	1.25	0.64
2M08510969+1159096	6026.4	6073.3	5957.1	4.18	−9999.	4.08	1.25	0.63
2M08511576+1152587	6093.1	6137.2	5960.3	4.18	−9999.	3.97	1.27	1.24
2M08512240+1151291	6009.8	6056.5	6056.2	4.20	−9999.	4.08	1.23	0.85
2M08513710+1154599	6110.2	6156.0	6052.5	4.29	−9999.	4.07	1.23	0.63

Table 2
(Continued)

2Mass ID	$T_{\rm eff}$ (K) ASPCAP raw	$T_{\rm eff}$ (K) ASPCAP calib	$T_{\rm eff}$ (K) GB09	log g (cm s^{-2}) ASPCAP raw	log g (cm s^{-2}) ASPCAP calib	log g (cm s^{-2}) Physical	Mass ($M_{\odot}$) Mass isochrone	ξ (km s^{-1}) ASPCAP raw
2M08513806+1201243	5882.2	5926.9	5845.0	4.16	−9999.	3.95	1.28	0.59
2M08514122+1154290	6118.1	6162.7	6008.6	4.19	−9999.	3.95	1.28	0.74
2M08514475+1145012	6040.5	6086.9	6136.3	4.36	−9999.	4.14	1.23	0.68
2M08520741+1150221	6043.8	6087.8	6057.0	4.29	−9999.	4.08	1.25	0.66
Main Sequence								
2M08502805+1154505	5759.3	5806.5	5755.8	4.17	−9999.	4.33	1.14	0.61
2M08511229+1154230	5848.9	5892.7	5885.6	4.35	−9999.	4.34	1.12	0.68
2M08512314+1154049	5802.4	5847.1	5886.3	4.27	−9999.	4.34	1.11	0.73
2M08512604+1149555	5310.1	5358.8	5472.1	4.08	−9999.	4.33	1.00	0.61
2M08512996+1151090	5900.8	5945.5	5925.8	4.34	−9999.	4.34	1.11	0.64
2M08513119+1153179	6062.9	6108.2	6021.5	4.30	−9999.	4.24	1.17	0.68
2M08513701+1136516	5201.7	5244.9	5211.6	4.52	−9999.	4.65	0.81	0.86
2M08514189+1149376	5481.9	5525.2	5595.9	4.31	−9999.	4.48	1.03	0.90
2M08514742+1147096	5199.1	5245.7	5226.8	4.24	−9999.	4.57	0.85	0.60
2M08521649+1147382	5467.4	5512.1	5573.0	4.33	−9999.	4.49	1.01	0.72
2M08505439+1156290	6163.0	6207.7	5956.9	4.29	−9999.	4.33	1.10	0.63
2M08510076+1153115	5564.3	5609.2	5798.0	4.25	−9999.	4.50	0.93	0.60
2M08511176+1150018	4857.4	4902.6	4779.6	4.20	−9999.	4.67	0.75	0.57
2M08512080+1145024	5799.6	5845.3	5998.8	4.28	−9999.	4.40	0.98	0.67
2M08512742+1153265	6169.5	6214.1	5998.8	4.31	−9999.	4.31	1.11	0.73
2M08512788+1155409	5834.3	5878.5	5860.8	4.30	−9999.	4.48	0.98	0.61
2M08513012+1143498	5866.0	5913.1	6036.4	4.36	−9999.	4.45	1.00	0.62
2M08513455+1149068	4922.6	4966.8	4908.2	4.45	−9999.	4.69	0.75	0.86
2M08521868+1143246	5960.3	6006.6	5970.8	4.19	−9999.	4.42	1.03	0.62
2M08512643+1143506	7985.2	−9999.0	7686.9	4.67	−9999.	4.53	1.21	1.55
2M08513259+1148520	7599.0	7647.2	7095.6	4.38	−9999.	4.44	1.21	2.82
Excluded sample due to low S/N (<100) Subgiant								
2M08503438+1139566	5955.8	5998.6	5947.6	4.11	−9999.	3.87	1.28	0.67
2M08504198+1136525	5597.0	5647.9	5611.6	3.92	−9999.	3.79	1.29	0.94
2M08510811+1201065	5625.6	5674.2	5679.9	4.02	−9999.	3.80	1.29	0.59
2M08511826+1150196	5458.1	5508.6	5454.3	4.01	−9999.	3.77	1.29	0.58
2M08520356+1141238	5954.6	6000.4	5984.7	4.07	−9999.	3.89	1.28	0.70
Main Sequence								
2M08502833+1142097	6164.8	6210.0	6060.1	4.28	−9999.	4.33	1.10	0.86
2M08503788+1252295	5362.5	5405.2	5381.2	4.39	−9999.	4.68	0.87	1.11
2M08505334+1143399	5194.7	5242.1	5536.2	4.22	−9999.	4.56	0.85	0.69
2M08505923+1146129	5567.1	5613.8	5943.0	4.21	−9999.	4.51	0.93	0.71
2M08512386+1138521	5614.1	5659.0	5789.1	4.47	−9999.	4.52	0.93	0.70
2M08513215+1136126	5935.4	5981.2	6132.1	4.33	−9999.	4.42	1.03	0.73
2M08513444+1137574	6000.8	6045.6	6003.4	4.24	−9999.	4.40	1.04	0.63
2M08514375+1145148	6056.9	6104.1	6127.2	4.30	−9999.	4.38	1.06	0.66
2M08514465+1141510	6091.1	6136.1	6031.7	4.39	−9999.	4.36	1.07	0.72
2M08515290+1146358	4624.6	4670.1	4633.9	4.34	−9999.	4.71	0.70	1.24
2M08521664+1142300	5985.2	6033.1	6122.4	4.28	−9999.	4.36	1.04	0.58
2M08504511+1136023	4547.0	4593.2	4640.2	4.17	−9999.	4.55	0.75	0.57
2M08510131+1141587	5904.2	5953.5	5906.2	4.24	−9999.	4.45	1.01	0.70
2M08510156+1147501	5642.9	5688.3	5749.4	4.17	−9999.	4.49	0.95	0.58
2M08511229+1146212	5806.2	5851.6	5856.3	4.25	−9999.	4.47	0.98	0.64
2M08511810+1142547	5895.8	5940.7	5920.0	4.27	−9999.	4.45	1.01	0.70
2M08512033+1145523	6063.8	6108.9	6146.6	4.32	−9999.	4.39	1.06	0.68
2M08512176+1144050	5360.8	5406.7	5624.3	4.26	−9999.	4.60	0.86	0.64
2M08512467+1143061	5219.1	5264.6	5446.2	4.39	−9999.	4.57	0.85	0.78
2M08513424+1145535	5193.5	5235.5	5174.0	4.62	−9999.	4.56	0.85	0.57

However, when we analyze the stars by class (main sequence, turnoff, subgiant, red giant), the scatter in the derived elemental abundance is drastically reduced to 0.03–0.04 dex for most of the elements. As our sample covers a wide range in surface gravity, $1.78 \leqslant \log g \leqslant 4.71$, it is possible that the observed scatter is the signature of a physical process modifying the stellar atmospheric

Table 3
Stellar Abundances

2Mass ID	[Fe/H]	[C/H]	[N/H]	[O/H]	[Na/H]	[Mg/H]	[Al/H]	[Si/H]	[K/H]	[Ca/H]	[Ti/H]	[V/H]	[Cr/H]	[Mn/H]	[Ni/H]
Red Giant															
2M08492491+1144057	0.13	−0.20	0.35	0.09	0.33	0.17	0.42	0.24	0.03	0.14	0.22	0.20	0.01	0.08	0.11
2M08503613+1143180	0.02	−0.07	0.14	0.04	0.08	0.02	0.18	0.13	−0.04	−0.01	−0.07	0.19	−0.01	−0.03	0.02
2M08504964+1135089	0.07	−0.16	0.43	0.09	0.32	0.11	0.32	0.21	0.00	0.06	0.04	0.28	−0.04	0.07	0.07
2M08511269+1152423	0.07	−0.16	0.29	0.11	0.32	0.13	0.47	0.26	−0.01	0.10	0.12	0.17	−0.04	0.08	0.03
2M08511704+1150464	0.07	−0.20	0.48	0.13	0.28	0.13	0.27	0.21	−0.03	0.06	0.08	−0.00	0.01	0.03	0.05
2M08511897+1158110	0.06	−0.20	0.38	0.13	0.14	0.07	0.26	0.19	−0.04	0.05	−0.02	0.09	−0.01	0.05	0.06
2M08512156+1146061	0.10	−0.15	0.35	0.12	0.31	0.14	0.34	0.24	0.01	0.09	0.06	0.26	0.01	0.08	0.09
2M08512618+1153520	0.06	−0.19	0.33	0.10	0.37	0.11	0.41	0.25	−0.05	0.06	0.08	0.14	−0.08	0.05	0.02
2M08512898+1150330	0.04	−0.08	0.21	0.09	0.35	0.10	0.34	0.24	−0.04	0.06	0.01	0.12	−0.08	0.06	0.03
2M08512990+1147168	−0.05	−0.14	0.39	0.05	0.35	0.07	0.31	0.11	−0.15	−0.03	0.02	−0.02	−0.06	−0.07	−0.07
2M08513577+1153347	0.04	−0.13	0.24	0.09	0.12	0.05	0.24	0.15	−0.06	0.01	0.02	0.14	−0.04	0.02	0.04
2M08513938+1151456	0.06	−0.18	0.30	0.12	0.22	0.08	0.36	0.19	0.00	0.05	0.07	0.21	−0.05	0.03	0.03
2M08514234+1150076	0.12	−0.17	0.44	0.21	0.31	0.26	0.32	0.23	−0.03	0.15	0.13	−0.06	0.00	0.05	0.08
2M08514388+1156425	0.07	−0.18	0.30	0.11	0.29	0.13	0.41	0.27	−0.02	0.07	0.06	0.14	−0.04	0.07	0.02
2M08514507+1147459	0.07	−0.14	0.29	0.11	0.33	0.10	0.34	0.21	−0.01	0.07	0.04	0.24	−0.00	0.03	0.04
2M08514883+1156511	0.04	−0.15	0.18	0.14	0.19	0.04	0.25	0.18	−0.10	0.03	−0.04	0.14	−0.10	−0.02	0.04
2M08515611+1150147	0.15	−0.17	0.09	0.15	0.27	0.18	0.42	0.28	0.02	0.19	0.14	0.37	0.05	0.08	0.10
2M08515952+1155049	0.04	−0.17	0.31	0.07	0.26	0.08	0.39	0.23	−0.06	0.04	−0.01	0.16	−0.05	0.02	−0.00
2M08521097+1131491	0.10	−0.16	0.35	0.17	0.32	0.17	0.43	0.26	0.02	0.13	0.14	0.22	0.01	0.08	0.05
2M08521656+1119380	0.03	−0.19	0.27	0.12	0.37	0.14	0.43	0.22	−0.03	0.09	0.09	0.04	−0.07	0.04	−0.02
2M08521856+1144263	0.06	−0.23	0.39	0.12	0.39	0.14	0.35	0.23	−0.05	0.05	0.05	0.34	−0.04	0.07	0.05
2M08522636+1141277	0.05	−0.19	0.33	0.20	0.17	0.10	0.25	0.20	−0.04	0.04	0.10	0.14	−0.04	−0.04	0.06
2M08525625+1148539	0.16	−0.21	0.31	0.31	0.29	0.21	0.43	0.31	0.07	0.15	0.23	0.21	0.08	0.12	0.16
2M08534672+1123307	0.11	0.03	0.11	0.05	0.31	0.13	0.38	0.29	0.05	0.09	0.10	0.28	0.04	0.04	0.12
2M08493465+1151256	−1.14	−0.72	0.68	−1.00	−2.50	−0.98	−0.63	−1.54	−0.72	−0.92	−1.43	−1.63	−1.90	−0.10	−0.97
2M08505816+1152223	0.08	−0.05	−0.01	0.03	0.26	0.09	0.28	0.20	−0.02	0.11	0.05	0.18	−0.01	0.05	0.09
2M08510723+1153019	−1.71	−0.69	−0.26	−0.15	−1.36	−2.21	−1.77	−2.21	−1.23	−1.53	−2.21	−0.84	−0.89	−1.21	−1.36
2M08510839+1147121	0.07	−0.15	−0.08	0.26	0.16	0.09	0.27	0.21	−0.01	0.06	−0.03	0.30	0.01	0.04	0.06
2M08522003+1127362	0.09	−0.10	−0.07	0.27	0.28	0.13	0.30	0.22	−0.03	0.09	0.07	0.15	−0.01	0.04	0.09
Subgiant															
2M08504994+1149127	−0.05	−0.02	0.20	−0.05	−0.07	−0.03	0.04	0.05	−0.09	−0.06	−0.10	−0.04	0.01	−0.11	−0.04
2M08510325+1145473	0.01	0.01	−0.02	0.07	−0.76	−0.25	−0.03	−0.02	−0.07	0.05	−0.04	−0.52	−2.35	−0.06	−0.01
2M08511564+1150561	0.04	−0.11	0.10	0.15	0.16	0.02	0.19	0.11	−0.00	0.00	−0.00	0.14	−0.07	0.02	0.07
2M08511670+1145293	0.01	−0.02	−0.00	0.04	0.24	−0.11	0.00	0.05	−0.05	0.02	0.03	−0.40	0.05	−0.02	−0.00
2M08512122+1145526	−0.05	−0.02	−0.05	0.02	−0.55	−0.24	−0.06	−0.11	−0.07	−0.06	−0.26	−0.36	−2.34	−0.10	−0.01
2M08512879+1151599	0.00	−0.04	−0.01	−0.02	0.29	−0.11	0.04	0.08	−0.19	−0.01	0.09	−0.02	−0.02	−0.13	−0.01
2M08512935+1145275	0.01	−0.14	0.16	0.08	0.24	0.00	0.12	0.12	−0.06	−0.01	−0.11	−0.14	−0.03	−0.02	0.01
2M08513540+1157564	0.01	−0.26	0.03	0.17	0.17	−0.08	0.11	0.03	−0.01	−0.06	−0.21	0.03	−0.07	−0.04	0.03
2M08513862+1220141	0.02	0.03	−0.03	0.09	0.17	0.01	0.13	0.08	−0.07	−0.04	−0.12	0.21	−0.03	0.01	0.06
2M08514401+1146245	0.07	0.01	0.15	−0.07	0.35	0.10	0.13	0.10	−0.03	−0.09	0.18	−0.39	0.01	0.05	0.05
2M08514474+1146460	−0.01	−0.17	0.14	0.11	0.19	−0.03	0.08	0.03	−0.09	−0.05	−0.12	0.09	−0.09	−0.02	0.03
2M08514994+1149311	−0.00	0.01	−0.01	0.12	−2.38	0.02	0.15	0.17	0.01	0.06	0.10	0.13	−2.25	−0.06	0.02
2M08515335+1148208	−0.06	−0.06	−0.07	0.05	−0.95	−0.04	0.10	0.07	−0.01	−0.01	0.06	0.04	−2.17	−0.12	−0.02
2M08521134+1145380	0.08	−0.07	0.29	0.03	0.39	0.10	0.07	0.12	−0.03	0.04	0.06	−0.29	−0.02	0.02	0.06
2M08503667+1148553	−0.07	−0.04	−0.06	−0.09	−1.34	−0.09	0.12	−0.02	0.05	0.01	0.03	−0.03	−2.38	−0.20	−0.07
2M08505569+1152146	0.01	0.02	−0.08	0.00	0.37	0.02	0.15	0.15	−0.03	0.01	−0.06	0.14	−0.26	−0.11	0.01
2M08510106+1150108	0.08	0.04	−0.08	0.34	0.15	0.08	0.16	0.18	−0.03	0.09	0.17	−0.04	0.08	0.04	0.06

Table 3
(Continued)

2Mass ID	[Fe/H]	[C/H]	[N/H]	[O/H]	[Na/H]	[Mg/H]	[Al/H]	[Si/H]	[K/H]	[Ca/H]	[Ti/H]	[V/H]	[Cr/H]	[Mn/H]	[Ni/H]
2M08510951+1141449	0.15	0.07	−0.04	0.25	0.23	0.13	0.23	0.27	0.01	0.16	0.22	−0.15	0.18	0.15	0.15
2M08511877+1151186	0.09	−0.08	−0.01	−0.06	0.17	0.08	0.28	0.15	0.04	0.08	0.04	0.21	−0.02	0.04	0.11
2M08515567+1217573	0.04	−0.07	−0.07	0.14	−2.20	0.03	0.20	0.14	−0.10	0.05	−0.04	0.09	0.01	−0.01	0.06
Turnoff															
2M08503392+1146272	0.01	0.01	⋯	⋯	⋯	−0.00	0.14	0.10	−0.05	−0.04	−0.31	0.01	⋯	−0.04	0.05
2M08504079+1147462	−0.05	−0.03	⋯	⋯	⋯	−0.04	0.07	0.13	−0.09	−0.03	0.22	−0.31	⋯	−0.18	−0.02
2M08505177+1200247	−0.03	−0.03	⋯	⋯	⋯	−0.22	−0.04	−0.10	−0.19	−0.09	−0.47	0.05	⋯	−0.09	−0.01
2M08505702+1159158	−0.08	−0.07	⋯	⋯	⋯	−0.26	−0.03	−0.13	0.03	−0.03	−0.06	−0.10	⋯	−0.14	−0.02
2M08505762+1155147	−0.02	−0.02	⋯	⋯	⋯	−0.08	0.04	0.06	−0.01	−0.05	−0.36	−0.10	⋯	−0.09	−0.00
2M08505903+1148576	−0.03	−0.02	⋯	⋯	⋯	−0.26	−0.10	−0.02	−0.03	−0.07	−0.53	0.03	⋯	−0.11	−0.05
2M08505973+1139524	−0.03	−0.02	⋯	⋯	⋯	−0.22	−0.08	0.01	−0.15	−0.02	−0.32	−0.35	⋯	−0.11	0.00
2M08510969+1159096	−0.11	−0.12	⋯	⋯	⋯	−0.34	−0.15	−0.15	−0.10	−0.09	−0.20	−0.28	⋯	−0.19	−0.12
2M08511576+1152587	−0.02	−0.00	⋯	⋯	⋯	−0.18	0.13	−0.04	0.06	0.02	0.01	−0.04	⋯	−0.05	0.04
2M08512240+1151291	−0.12	−0.11	⋯	⋯	⋯	−0.28	−0.18	−0.17	−0.06	−0.16	−0.22	0.03	⋯	−0.16	−0.05
2M08513710+1154599	−0.01	−0.07	⋯	⋯	⋯	−0.15	−0.03	0.05	−0.10	0.11	−0.11	−0.15	⋯	−0.10	0.06
2M08513806+1201243	−0.01	−0.04	⋯	⋯	⋯	−0.25	−0.10	−0.06	−0.02	0.11	−0.28	−0.05	⋯	−0.12	0.04
2M08514122+1154290	−0.04	−0.03	⋯	⋯	⋯	−0.22	−0.01	−0.06	−0.01	−0.05	−0.49	0.04	⋯	−0.12	−0.00
2M08514475+1145012	−0.10	−0.08	⋯	⋯	⋯	−0.32	−0.19	−0.11	−0.04	−0.14	−0.14	0.26	⋯	−0.13	−0.06
2M08520741+1150221	−0.00	−0.01	⋯	⋯	⋯	−0.13	0.05	0.02	−0.12	0.02	−0.36	−0.10	⋯	−0.03	0.02
Main Sequence															
2M08502805+1154505	0.02	−0.00	⋯	⋯	⋯	−0.10	0.02	−0.08	−0.03	0.06	0.12	−0.12	⋯	−0.06	−0.03
2M08511229+1154230	0.04	0.01	⋯	⋯	⋯	−0.08	0.01	0.03	0.06	0.06	−0.00	0.06	⋯	−0.04	0.05
2M08512314+1154049	0.00	−0.04	⋯	⋯	⋯	−0.17	−0.08	−0.01	−0.01	0.05	−0.49	0.04	⋯	−0.12	0.01
2M08512604+1149555	−0.02	−0.13	⋯	⋯	⋯	−0.05	0.15	−0.08	−0.01	0.03	0.03	0.02	⋯	−0.12	−0.02
2M08512996+1151090	−0.01	−0.03	⋯	⋯	⋯	−0.14	−0.04	−0.00	0.01	0.04	−0.07	0.03	⋯	−0.05	0.03
2M08513119+1153179	−0.03	−0.03	⋯	⋯	⋯	−0.19	−0.10	−0.04	−0.07	−0.06	−0.19	0.04	⋯	−0.07	−0.01
2M08513701+1136516	0.03	0.06	⋯	⋯	⋯	0.03	0.02	0.04	−0.01	0.01	0.12	0.15	⋯	0.03	0.07
2M08514189+1149376	0.06	0.02	⋯	⋯	⋯	−0.10	−0.09	0.12	−0.05	0.14	−0.11	0.07	⋯	0.02	0.11
2M08514742+1147096	0.05	−0.03	⋯	⋯	⋯	0.00	0.03	0.01	−0.00	0.02	0.01	0.08	⋯	0.03	0.03
2M08521649+1147382	0.02	−0.04	⋯	⋯	⋯	−0.15	−0.06	0.07	−0.03	0.05	−0.33	0.13	⋯	−0.01	0.07
2M08505439+1156290	−0.04	−0.02	⋯	⋯	⋯	−0.21	−0.01	−0.08	−0.11	−0.08	−0.11	−0.04	⋯	−0.10	0.04
2M08510076+1153115	0.02	−0.02	⋯	⋯	⋯	−0.13	0.10	0.04	−0.02	−0.03	−0.08	0.11	⋯	−0.05	0.05
2M08511176+1150018	0.03	−0.01	⋯	⋯	⋯	−0.32	−0.10	0.04	−0.09	0.12	−0.07	0.10	⋯	−0.05	0.04
2M08512080+1145024	−0.03	−0.03	⋯	⋯	⋯	−0.21	−0.12	−0.02	−0.24	0.03	−0.20	−0.84	⋯	−0.13	−0.04
2M08512742+1153265	−0.04	−0.03	⋯	⋯	⋯	−0.15	0.01	−0.03	−0.01	−0.01	−0.04	−0.02	⋯	−0.07	0.02
2M08512788+1155409	−0.03	−0.02	⋯	⋯	⋯	−0.20	−0.01	−0.11	0.02	0.01	−0.09	0.04	⋯	−0.07	0.09
2M08513012+1143498	−0.07	−0.06	⋯	⋯	⋯	−0.28	−0.19	−0.06	−0.25	−0.05	−0.56	−0.75	⋯	−0.17	−0.07
2M08513455+1149068	0.06	0.02	⋯	⋯	⋯	−0.12	0.01	0.09	−0.01	0.13	0.05	0.06	⋯	−0.01	0.09
2M08521868+1143246	−0.08	−0.05	⋯	⋯	⋯	−0.35	−0.14	−0.07	−0.08	−0.10	−0.17	0.21	⋯	−0.21	−0.10
2M08512643+1143506	−0.21	−0.67	⋯	⋯	⋯	−0.16	−1.56	0.26	0.13	0.58	−0.66	−2.11	⋯	0.54	0.04
2M08513259+1148520	−0.18	−0.15	⋯	⋯	⋯	−0.17	−0.46	0.02	−0.60	−0.61	−0.55	−0.61	⋯	−0.19	−0.15
Excluded sample due to low S/N (<100)															
Subgiant															
2M08503438+1139566	0.10	0.07	0.06	0.09	0.72	0.03	0.24	0.25	−0.05	0.20	0.16	−0.08	−0.25	−0.08	0.08
2M08504198+1136525	0.11	0.03	0.07	0.03	0.33	0.08	0.11	0.34	0.02	0.26	0.24	−0.04	0.00	−0.01	0.12
2M08510811+1201065	−0.07	−0.13	−0.12	−0.32	⋯	−0.13	0.36	0.03	−0.09	0.18	0.29	−0.26	⋯	−0.18	−0.05

Table 3
(Continued)

2Mass ID	[Fe/H]	[C/H]	[N/H]	[O/H]	[Na/H]	[Mg/H]	[Al/H]	[Si/H]	[K/H]	[Ca/H]	[Ti/H]	[V/H]	[Cr/H]	[Mn/H]	[Ni/H]
2M08511826+1150196	−0.17	−0.21	−0.20	−0.39	⋯	−0.29	0.07	−0.12	−0.15	−0.03	−0.12	−0.24	⋯	−0.30	−0.21
2M08520356+1141238	−0.04	−0.02	−0.05	0.01	−0.56	0.04	0.08	0.11	0.05	−0.01	0.20	0.09	−0.22	−0.27	0.01
Main Sequence															
2M08502833+1142097	0.01	−0.02	⋯	⋯	⋯	−0.20	−0.05	0.16	0.05	0.05	0.27	−0.05	⋯	0.05	0.09
2M08503788+1252295	0.07	0.04	⋯	⋯	⋯	−0.18	−0.05	0.08	−0.03	0.12	−0.06	0.07	⋯	−0.01	0.14
2M08505334+1143399	−0.10	−0.13	⋯	⋯	⋯	−0.60	−0.11	−0.07	−0.36	0.04	−0.41	−0.50	⋯	−0.18	−0.05
2M08505923+1146129	−0.10	−0.11	⋯	⋯	⋯	−0.43	−0.47	−0.18	−0.18	−0.07	−0.14	−0.85	⋯	−0.10	−0.04
2M08512386+1138521	−0.04	−0.07	⋯	⋯	⋯	−0.25	−0.14	−0.09	−0.10	−0.10	−0.47	0.07	⋯	−0.10	0.02
2M08513215+1136126	−0.05	−0.03	⋯	⋯	⋯	−0.20	−0.16	−0.14	−0.06	−0.32	0.48	−2.50	⋯	0.04	0.01
2M08513444+1137574	0.02	0.02	⋯	⋯	⋯	−0.28	−0.10	0.01	−0.24	0.05	0.35	0.75	⋯	−0.04	−0.02
2M08514375+1145148	−0.04	−0.08	⋯	⋯	⋯	−0.22	−0.17	−0.02	0.06	−0.05	0.21	0.41	⋯	0.00	0.00
2M08514465+1141510	−0.02	0.02	⋯	⋯	⋯	−0.19	−0.19	0.03	−0.07	0.03	0.17	0.43	⋯	−0.16	−0.00
2M08515290+1146358	0.12	0.02	⋯	⋯	⋯	−0.15	−0.11	0.25	−0.05	0.22	0.23	0.38	⋯	0.02	0.07
2M08521664+1142300	−0.15	−0.10	⋯	⋯	⋯	−0.31	−0.16	−0.13	0.22	−0.16	0.04	0.29	⋯	−0.29	−0.09
2M08504511+1136023	0.05	−0.08	⋯	⋯	⋯	−0.34	−0.34	0.12	0.04	0.03	−0.13	−0.27	⋯	−0.08	−0.15
2M08510131+1141587	−0.17	−0.19	⋯	⋯	⋯	−0.42	−0.23	−0.13	−0.39	−0.11	−0.43	−0.36	⋯	−0.23	−0.10
2M08510156+1147501	−0.09	−0.06	⋯	⋯	⋯	−0.42	−0.08	−0.25	−0.10	−0.06	−0.07	−0.54	⋯	−0.17	−0.00
2M08511229+1146212	−0.05	−0.02	⋯	⋯	⋯	−0.29	−0.08	−0.12	−0.14	0.05	−0.03	−0.40	⋯	−0.04	0.01
2M08511810+1142547	−0.02	0.01	⋯	⋯	⋯	−0.22	−0.09	−0.06	−0.14	−0.03	−0.32	−0.82	⋯	−0.07	−0.01
2M08512033+1145523	−0.03	−0.01	⋯	⋯	⋯	−0.21	−0.06	−0.01	−0.22	0.01	0.03	−0.32	⋯	−0.05	−0.03
2M08512176+1144050	−0.05	−0.06	⋯	⋯	⋯	−0.48	−0.12	−0.10	−0.10	0.09	−0.07	−0.10	⋯	−0.10	−0.09
2M08512467+1143061	0.03	0.01	⋯	⋯	⋯	−0.47	−0.05	0.13	−0.34	0.11	−0.38	0.21	⋯	−0.16	−0.07
2M08513424+1145535	0.06	0.03	⋯	⋯	⋯	−0.03	0.10	0.04	−0.01	0.13	0.08	0.14	⋯	0.02	0.09

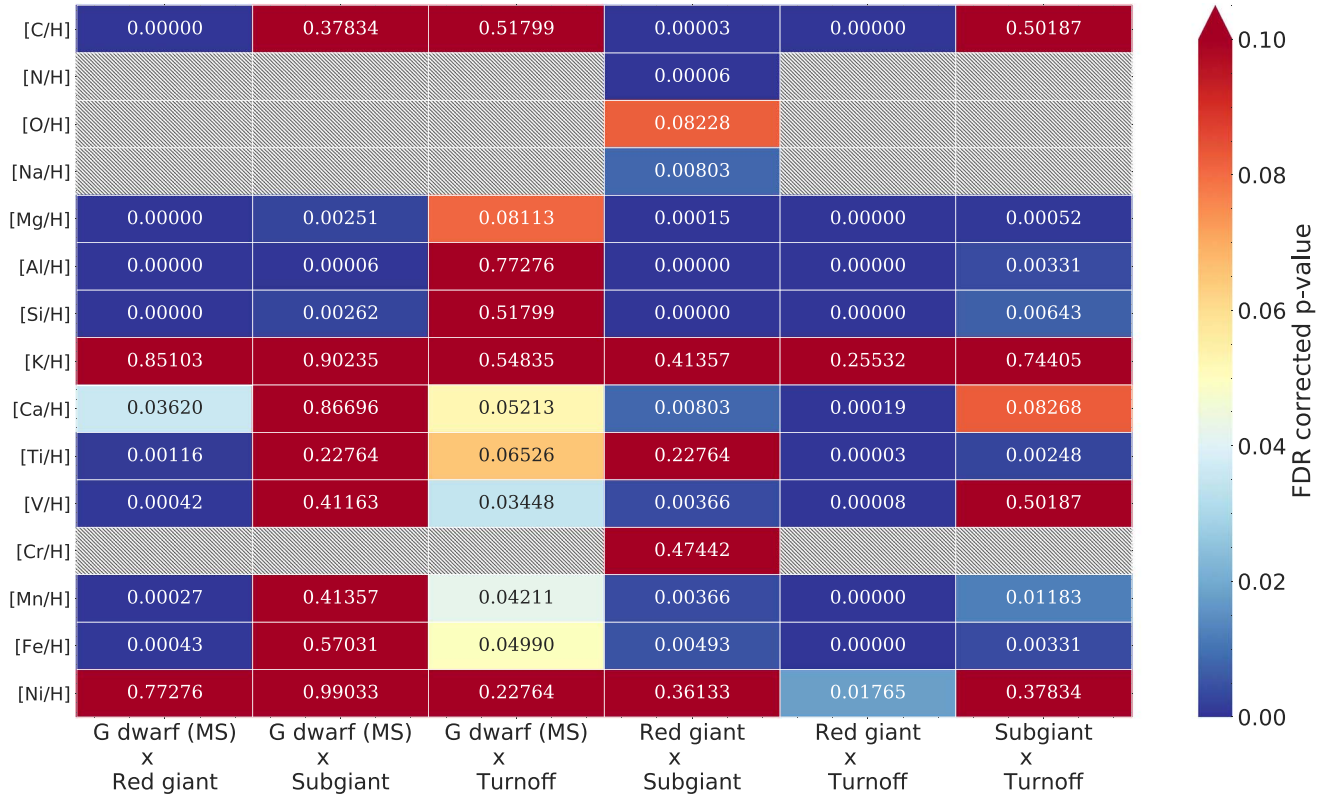

Figure 4. Kolmogorov–Smirnov test for the different elements (y axis) on the different stellar classes (x axis). The obtained p value is color coded from blue to red. The red colors are saturated at 0.1.

abundances, such as atomic diffusion as proposed by Souto et al. (2018). In the following sections, we discuss in detail the abundance trends as a function of the stellar parameters.

4.1. Abundance Variations across the H-R Diagram in M67 Stars

We split our sample into four different classes based on the stars' evolutionary stage. We selected as main-sequence stars those with $\log g \geqslant 4.20$, turnoff stars those with surface gravity $3.90 < \log g < 4.20$, subgiants those having $3.60 \leqslant \log g \leqslant 3.90$, and red giant stars those with $\log g < 3.60$. (We note that the cut in surface gravity is similar to the one in color and magnitude, as can be seen in the right panel of Figure 1.)

Probing the level of homogeneity in open clusters is important to understanding their formation and for evaluating the possibility of performing chemical tagging in stellar populations. Chemical homogeneity in open clusters (as well as in globular clusters) is a critical assumption to understand changes in the abundances across evolutionary stages. Bovy (2016) and Price-Jones & Bovy (2018), using APOGEE spectra, found tight constraints on the chemical homogeneity of M67 using a sample of red giant stars. Bovy (2016) analyzed 24 red giant stars in M67, finding one-dimensional sequences with a spread in the elemental initial cluster abundances lower than 0.03 dex (2σ of uncertainty) for all elements studied in this work. It is worth noting that the Bovy (2016) results were derived in a way that is insensitive to the effects of atomic diffusion, mixing, and other physical processes that may modify the stellar surface abundances.

One straightforward way to evaluate if samples of stars have similar abundances is to apply a Kolmogorov–Smirnov test (K-S test). The K-S test is usually invoked to find out if two samples are drawn from the same distribution. We perform a study of chemical homogeneity of M67 stars using the derived abundances through a K-S test, and we apply it to the same classes, for example, red giants × red giants. To be able to compare the derived abundances for the same classes using the K-S test, we randomly split each group into two samples and then we apply the K-S test. To ensure we do not choose a random split that favors homogeneity, for each group, we have run the test in 1000 random splits. This result shows that the abundances of each stellar class are indistinguishable, with the derived median p value >0.50 for all elements in the four stellar classes. This is a complementary result to Bovy (2016), finding chemical homogeneity of M67 stars in the same evolutionary stage based on the stellar abundances derived in this work.

We also applied the K-S test using the derived abundances for the 15 studied elements comparing stars in the different groups: G dwarf main sequence (MS) × red giant, G dwarf (MS) × subgiant, G dwarf (MS) × turnoff, red giant × subgiant, red giant × turnoff, and subgiant × turnoff stars.

In Figure 4 we present the results of the K-S two-sided test comparing the individual abundances for each stellar class. The vertical axis represents the [X/H] derived here, and the horizontal axis represents the subgroups being compared. Each cell shows the p value of the K-S test and is colored as shown in the side color bar. We designed the color scale to give a blue color if the samples are clearly distinct, a yellow color if the p

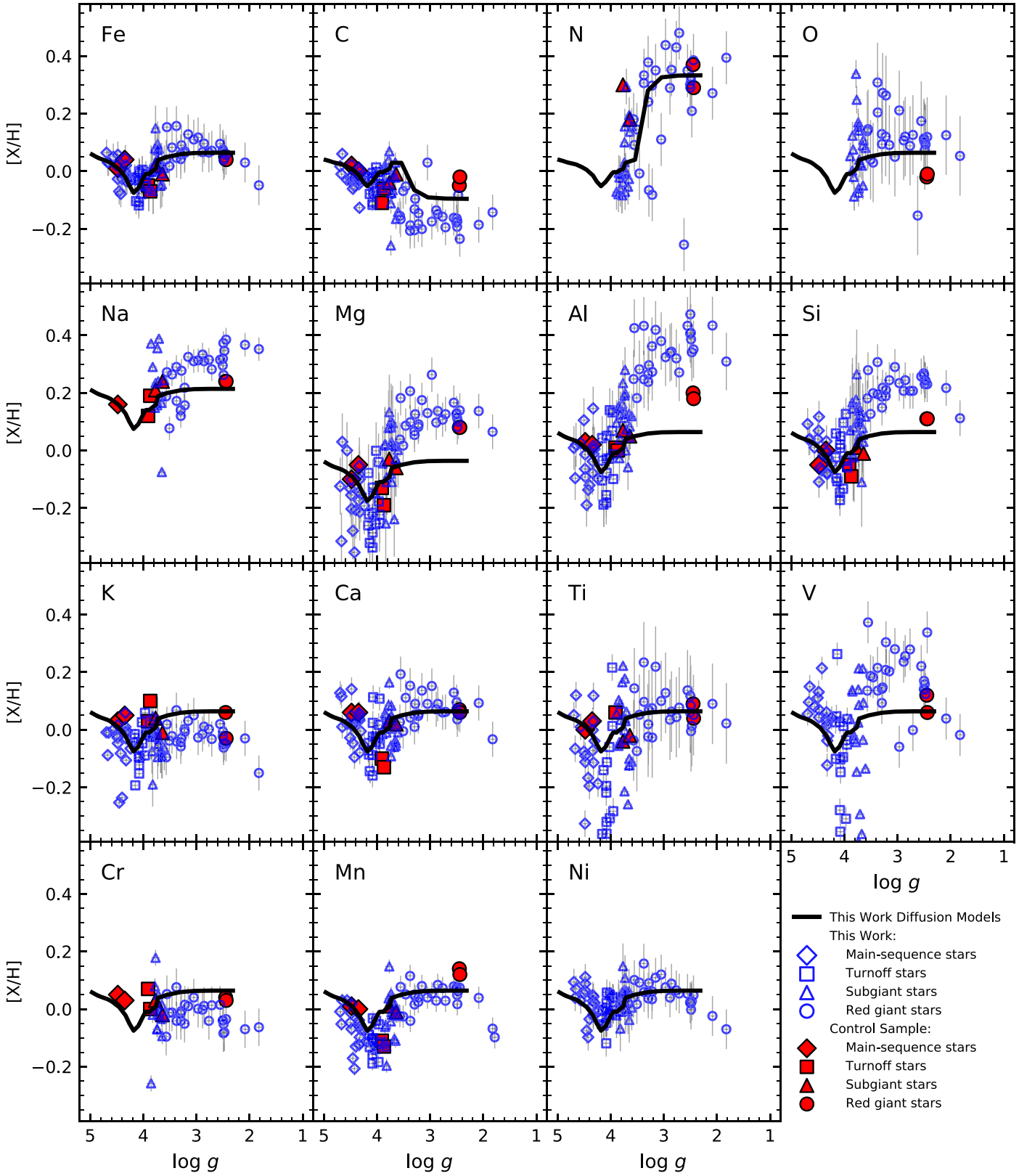

Figure 5. Chemical abundances for the studied stars are shown as a function of log g. The symbol notation is similar to Figure 1 (open symbols instead of filled symbols). The diffusion models calculated in this work are shown as solid black lines.

value is near 0.05, and a red color if we cannot reject the null hypothesis, that is, the samples are not distinguishable. Note that we have applied a false discovery rate (Benjamini & Hochberg 1995) correction in order to account for the fact that we are performing many hypothesis tests simultaneously, and spurious rejections of the null hypothesis are therefore expected. Regardless of the threshold that we use, we obtain outstanding segregation for red giant and turnoff stars based on

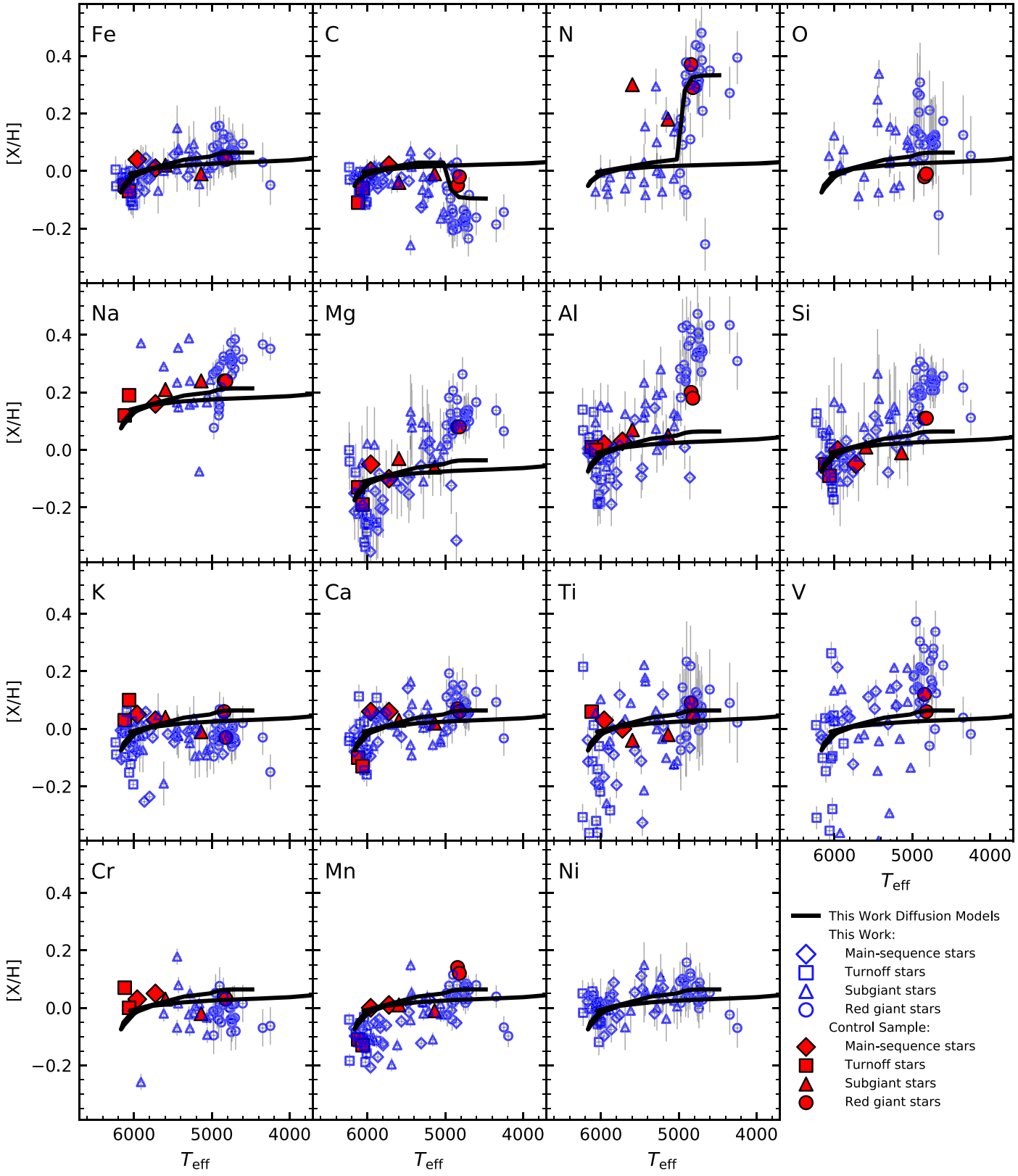

Figure 6. Same as Figure 5, except shown as a function of $T_{\rm eff}$.

their abundances. The K abundance is the one with higher p values (>0.03) for all scenarios. On the other hand, the two classes most difficult to separate based on their abundances are the main-sequence and the turnoff stars. The abundances of Mg, Ca, V, and Fe are the best ones to distinguish between these classes. The Mg abundances show significant differences among all stellar classes (with p values <0.10 for all comparisons).

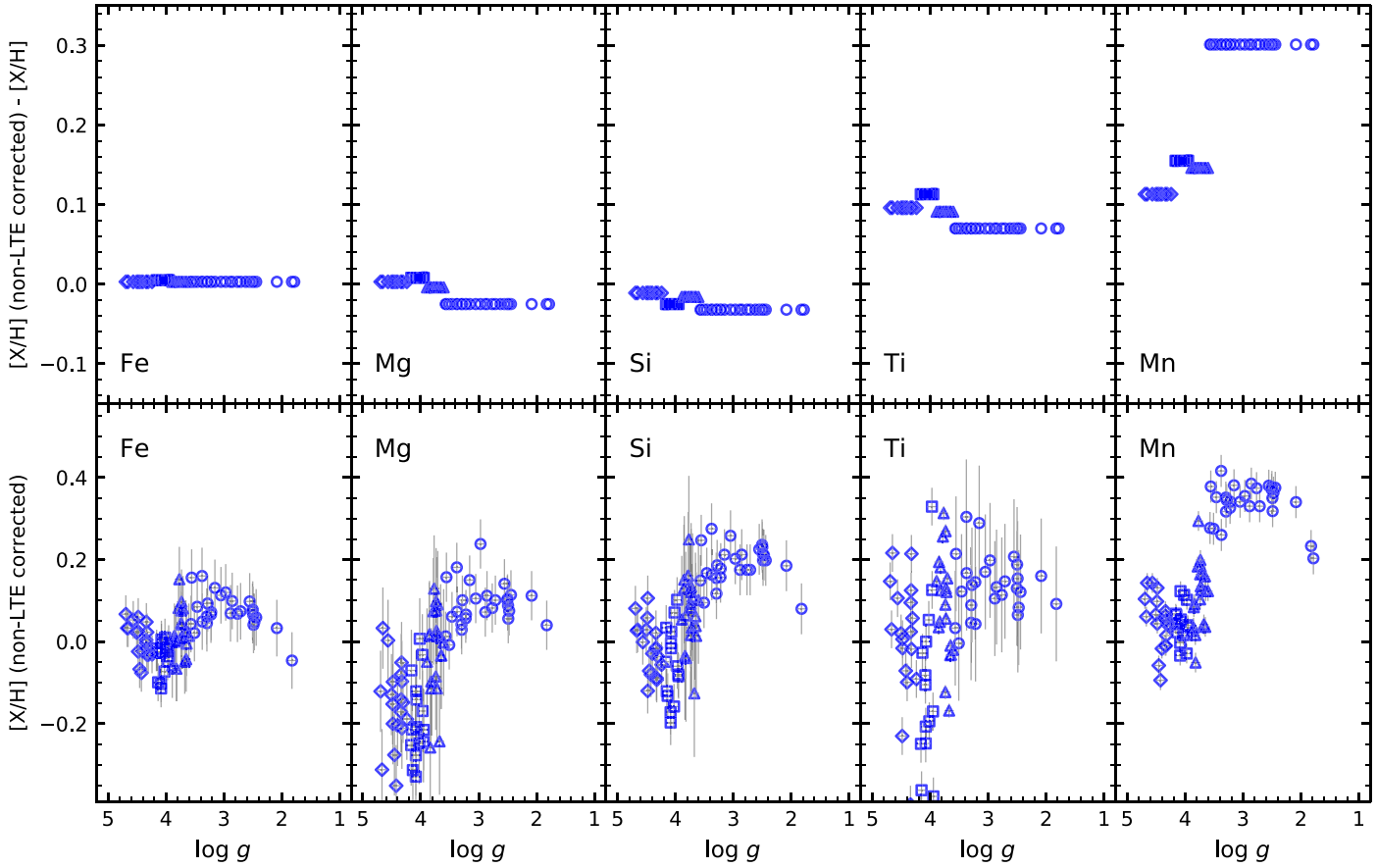

Figure 7. Top panel: log g vs. [X/H] (corrected-derived) individual abundances from non-LTE deviation. Bottom panel: log g vs. [X/H] corrected from non-LTE deviations. In both panels, the symbols follow the same notation as Figure 5.

4.1.1. As a Function of Stellar Parameters

In Figure 5 we display the derived individual abundances as a function of surface gravity for the 15 elements studied. We use the same symbol notation as in Figure 1, but with open symbols instead of filled. We also show the line-by-line manual abundance results from Souto et al. (2018), our control sample. Atomic diffusion models computed for this work (see Section 6) are overplotted for each element (C and N including mixing processes). We note that the diffusion models for Na and Mg abundances were slightly shifted in order to better fit the observed abundances.

From visual inspection—and in agreement with the results from the K-S test—we can organize the element variations as a function of surface gravity (as well as $T_{\rm eff}$ and $M_{\star}$) into three groups of elements: (1) C and N, with abundances displaying a different behavior for the evolved subgiant and red giant stars (as a consequence of dredge-up mechanisms); (2) O, Na, and Cr as their abundances are not reliable for the main-sequence and turnoff stars because their spectral lines become too weak; (3) the elements showing a dip, either sinuous or small, in the elemental abundance close to $\log g = 4.00$ dex (Fe, Mg, Al, Si, K, Ca, Ti, V, Mn, and Ni). The derived abundances of Mg, Al, and Si present the most significant changes between the stellar classes (excluding N), where the red giant abundances are 0.10 to 0.20 dex higher than those from the subgiants.

In Figure 6, we present the abundance results as a function of $T_{\rm eff}$ in M67 stars, with diffusion models also shown. Overall, the behavior seen in Figure 6 indicates an abundance increase (in the range 0.00–0.40 dex) as $T_{\rm eff}$ decreases from 6000 to 4000 K. The elements showing a smooth increase or decrease in abundance as functions of $T_{\rm eff}$ are Fe, Ca, and Mn. The elements most sensitive to $T_{\rm eff}$, Na, Mg, Al, and Si, show a monotonic increase in their individual abundances. Similar to the trends with log g, C shows a particular behavior, and the abundance variation of N shows a maximum value around $T_{\rm eff} \sim 4700$ K and then decreases for higher and lower values of $T_{\rm eff}$. The elements presenting the least sensitivity to $T_{\rm eff}$ are K, Cr, and Ni. Ti and V show the most significant abundance scatter in the analysis as a function of both log g and $T_{\rm eff}$.

Souto et al. (2018) showed that atomic diffusion processes can explain the abundance variations of M67 stars across the different evolutionary stages. However, other physical processes are also relevant in the context of abundance variations, where the most significant sources of deviations, not precisely in order, are non-LTE effects, 1D or 3D treatment of the model atmosphere, stellar rotation ($v \sin i$), mixing process (e.g., first dredge-up), and atomic diffusion processes. In the following sections, we discuss the impact of these possible deviations in our results.

5. Possible Explanations for the Abundance Trends

Figures 5 and 6 show significant abundance variations as a function of the stellar parameters (log g and $T_{\rm eff}$). Such abundance trends are not expected to occur in open clusters —due to the homogeneity of the stars formed by the same material—unless some additional effect or mechanism is playing a role in the stellar atmosphere, or in the abundance determination itself.

5.1. Non-LTE Deviations in the Near Infrared

Deviations from the LTE have been studied mostly at optical wavelengths, where strong deviations are found to occur in metal-poor, evolved red giant stars (Asplund 2005; Asplund et al. 2009). In the near infrared (NIR), in particular in the *H* band, the works of Cunha et al. (2015) and Zhang et al. (2016, 2017) have investigated non-LTE effects in Na I, Mg I, and Si I lines in the APOGEE spectra, finding deviations from non-LTE in these elements to be usually smaller than 0.05 dex (see also the discussion in Souto et al. 2018). Using the results from Bergemann & Gehren (2008) and Bergemann et al. (2012a, 2013, 2015) compiled from a Maria Bergemann website (nlte.mpia.de), we created a grid of non-LTE deviations for five elements: Fe, Mg, Si, Ti, and Mn. The deviations were estimated for each stellar class, assuming a solar metallicity and $T_{\rm eff} = 4700$ K, $\log g = 2.40$, and $\xi = 1.60\,{\rm km\,s^{-1}}$ for red giants; $T_{\rm eff} = 5400$ K, $\log g = 3.70$, and $\xi = 1.25\,{\rm km\,s^{-1}}$ for subgiants; $T_{\rm eff} = 6100$ K, $\log g = 3.90$, and $\xi = 1.15\,{\rm km\,s^{-1}}$ for turnoff stars; and $T_{\rm eff} = 5850$ K, $\log g = 4.40$, and $\xi = 1.00\,{\rm km\,s^{-1}}$ for main-sequence stars. We adopted 1D plane-parallel models computed with MAFAGS-OS for all stellar classes. In Table 4 we summarize the average non-LTE correction for each stellar class and element.

In Figure 7 we show the non-LTE corrected abundances for the five elements studied (Fe, Mg, Si, Ti, and Mn). The top panel displays the abundance differences from $[{\rm X/H}]_{\rm non\text{-}LTE}$–$[{\rm X/H}]_{\rm LTE}$, and in the bottom panel we show a plot similar to Figure 5, but now using the $[{\rm X/H}]_{\rm non\text{-}LTE}$.

The iron abundances do not show significant non-LTE deviations, as seen in Table 4, where δ(non-LTE–LTE) are smaller than 0.01 dex for all stellar classes. For Mg and Si, the deviation is very similar for main-sequence stars, both positive, being almost null for Mg. For subgiant and red giant stars, we obtain small, negative non-LTE corrections. The deviations for Ti and Mn are more significant in this study. For Ti, the deviations are positive for the stellar classes studied here, with the major deviation observed in turnoff stars (δ(non-LTE–LTE) = 0.11 dex). When applying non-LTE corrections, we do not see a strong change in the abundance versus log *g* diagram, when compared to the LTE one presented in Figure 5. The abundances of Ti are shifted in all classes, resulting in a higher scatter as a function of log *g*. The Mn corrections show the most significant differences, δ(non-LTE–LTE) $\sim$ 0.13 dex for main sequence, turnoff, and subgiants, and δ(non-LTE–LTE) $\sim$ 0.30 dex for red giants. The inclusion of non-LTE corrections in the analysis does not erase the observed abundance trends in the different stellar classes.

5.2. 1D or 3D Model Atmospheres

Stellar atmospheres are 3D and time-dependent; however, by convenience, we usually treat model atmospheres as having 1D plane-parallel or spherical geometry in hydrostatic equilibrium. This approximation simplifies the analysis, but can lead to systematic errors in the derived quantities (atmospheric parameters or chemical abundances).

The use of a 1D treatment of the stellar atmosphere requires the inclusion of "ad hoc" parameters to account for velocities that broaden the profiles at microscopic (microturbulence) and macroscopic (macroturbulence) levels. A precise determination of the microturbulence parameter minimizes the deviations from the results obtained with 3D models.

Table 4
Non-LTE Corrections

Stellar Class	Mg	Si	Ti	Mn	Fe
Main sequence	+0.003	−0.011	+0.096	+0.113	+0.003
Turnoff	+0.008	−0.025	+0.113	+0.155	+0.005
Subgiant	−0.004	−0.016	+0.091	+0.146	+0.003
Red giant	−0.025	−0.032	+0.070	+0.301	+0.003

As in non-LTE studies, 3D effects are also transition dependent, and analyses for NIR *H*-band transitions have been limited. The studies of Asplund (2005), Asplund et al. (2009), and Caffau et al. (2011) have summarized various effects and corrections for elemental abundances using optical spectra as a reference. In this section, we will summarize these effects for solar-metallicity stars to verify whether the abundance trends discussed in Section 4 could be explained by 3D effects.

Caffau et al. (2011) determined solar abundances from a 3D non-LTE analysis using the CO^{5}BOLD code, providing 3D abundance corrections for several elements. For Fe, Caffau et al. (2011) find 3D corrections to be about 0.03 dex using the solar spectrum. The C abundance reported by Caffau et al. (2011) has a −0.02 dex 3D correction, while for K the authors obtain a correction of 0.07 dex. From Caffau et al. (2009), the solar N abundance is reported to have a 3D correction smaller than 0.01 dex.

The previous work by Bergemann et al. (2012b) studied the 3D deviations for stars in different evolutionary stages at different metallicities. They find 3D effects in the iron abundance for the Sun to be very small: 3D corrections $\sim$0.01 dex. More recently, Bergemann et al. (2017) studied the Mg abundances in the Sun and found 3D corrections to be $\sim$0.02 dex. Amarsi & Asplund (2017) studied non-LTE 3D Si abundances in the Sun and found corrections to be lower than 0.01 dex. Amarsi et al. (2016), analyzing the O I forbidden line at 630 nm, find 3D corrections to the O abundance to be between 0.05 and 0.20 dex, negative in the Sun and reaching higher values for turnoff stars.

All 3D corrections discussed above are smaller than 0.05 dex (except for K), which is at the limit of the measurement uncertainties of this work. Given the small 3D corrections found for main-sequence stars, as well as the lack of studies in the literature for turnoff, subgiants, and red giant stars at solar metallicity, we conclude that deviations from 3D modeling are not enough to explain the abundance trends observed in this work.

5.3. Stellar Rotation

The study of the relation between stellar rotation and abundance variations in late-type stars is often motivated by the investigation of lithium depletion. Several authors have found correlations between stellar rotation and the lithium abundance depletion, such as Balachandran (1990, 1995), King et al. (2000), da Silva et al. (2009), Canto Martins et al. (2011), and Delgado Mena et al. (2014). None of the spectra analyzed in this study exhibit measurable rotational broadening ($v \sin(i)$) above the limits set by the APOGEE spectral resolution of $\sim$7–8 km s^{-1}.

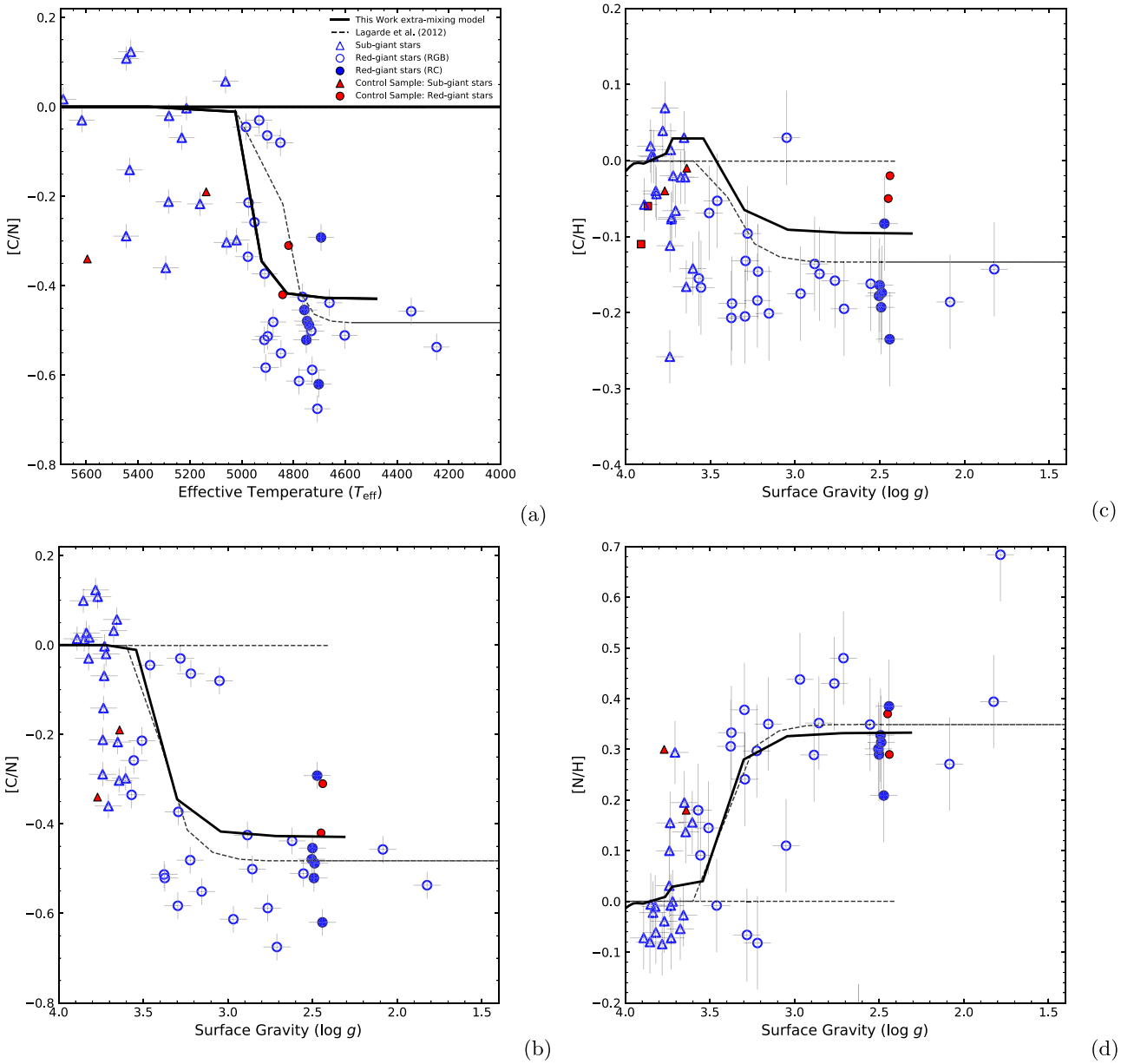

Figure 8. Panels (a) and (b) show $T_{\rm eff}$ vs. [C/N] and log g vs. [C/N], respectively. Panels (c) and (d) present the [C/H]–log g and [N/H]–log g diagrams. We display the mixing models from this work (solid black curve) and from Lagarde et al. (2012, dashed black curve) as a comparison. All symbols follow the same notation as Figure 5, with the inclusion of filled circles for the red clump stars.

6. Discussion

The abundance results obtained for M67 stars show evidence that both mixing and atomic diffusion are operating, so stellar evolution models that include diffusion will be compared to the observationally derived abundances.

6.1. Stellar Evolution Models

We computed our mixing and atomic diffusion models using solar models (solar metallicity and solar age 4 Gyr) to calibrate the degree of gravitational settling precisely (using the surface solar He as a proxy); this gives a predicted reduction in the efficiency of the settling of 15%, or an effective coefficient of 0.85. The methodology adopted in the modeling of mixing and atomic diffusion is described in detail in Bahcall et al. (2001) and Delahaye & Pinsonneault (2006). We note that, overall, our models agree with the ones from MIST (Choi et al. 2016, Dotter et al. 2017); however, our models cover all of the species studied in this work, while the MIST models are not available for Al, K, V, Cr, Mn, and Ni.

6.2. Mixing Processes: First Dredge-up

When a low-mass star, such as a $\sim 1.2 M_{\odot}$ M67 star that is currently evolving off of the main sequence and across the subgiant branch, reaches the base of the RGB, the outer convective envelope reaches its largest extent in mass. At this point in the H-R diagram (where $T_{\rm eff} \sim 5000$ K and $\log g \sim 3.5$ in M67), the base of the convective envelope ingests material that has been exposed previously to H burning via the CN cycle. As a consequence of CN-cycle H burning, this nuclear-processed material contains an enhanced abundance of ^{14}N and a decreased abundance of ^{12}C. The convective envelope will carry this mixture to the surface, resulting in a lower surface

abundance of ^{12}C and a larger abundance of ^{14}N for stars evolving onto the RGB; this phase of stellar evolution is referred to as first dredge-up, or FDU (Iben 1965; for a more recent overview of the various red giant dredge-up episodes, see Karakas & Lattanzio 2014). In the case of dredge-up in M67 red giants, the ^{14}N abundance is predicted to be enhanced by roughly $\sim+0.30$ to $+0.40$ dex, while the ^{12}C abundance is predicted to be depleted by ~-0.10 to -0.20 dex. The magnitudes of the abundance changes in C and N are a function of red giant mass (Iben 1965), with larger-mass stars having deeper convective envelopes that dredge up more nuclear-processed material, resulting in larger ^{14}N enhancements and larger ^{12}C depletions, producing lower C/N ratios.

The expected relationship between red giant mass and C/N ratio has been exploited by a number of recent studies using APOGEE data and results (e.g., Martig et al. 2016; Ness et al. 2016; see also D. Feuillet et al. 2019, in preparation) to produce age–mass relations as a function of red giant [C/N] abundances, while Masseron & Gilmore (2015) have analyzed [C/N] to study the possible formation of the thin and thick disk.

In addition to standard convection in 1D, other physical processes can modify the interior abundance profiles in stars as they evolve from the main sequence, across the subgiant branch, and onto the RGB, with two important processes being rotation and the inversion of the mean molecular weight gradient in a small region outside the H-burning shell created by ^{3}He burning via ^{3}He(^{3}He, 2p)α (Eggleton et al. 2006; Charbonnel & Zahn 2007); this last process is referred to as thermohaline mixing. The inclusion of rotation-induced mixing and thermohaline mixing produces larger carbon depletions and larger nitrogen enhancements as a result of FDU. In this section, we use ^{12}C and ^{14}N abundances derived here to compare with predictions from various models of first dredge-up mixing.

As shown in Figure 8, the M67 red giants display clear evidence of the first dredge-up through the behavior of the C and N abundances as functions of both $T_{\rm eff}$ and $\log g$ (which map the position of a star along the subgiant and RGB); observed APOGEE abundances are plotted as the various symbols, while models are plotted as the continuous lines and are models from this study, along with those from Lagarde et al. (2012). The left panels of Figure 8 plot the [C/N] values versus $T_{\rm eff}$ (top, (a)) and $\log g$ (bottom, (b)), with the [C/N] values decreasing rapidly at $T_{\rm eff}\sim 5000$ K and $\log g\sim 3.5$, right at the base of the RGB as predicted by FDU. The right panels plot the individual abundances of ^{12}C (as [C/H]) and ^{14}N (as [N/H]) versus $\log g$. Carbon and nitrogen abundance differences between red giants on the RGB relative to those in the RC were found to agree with results from Tautvaišiene et al. (2000) and Masseron et al. (2017), who found slightly lower values of C/N in RC stars compared to those on the RGB. Our values for M67 stars are $\langle {}^{12}{\rm C}/{}^{14}{\rm N}\rangle_{\rm RGB} = 1.86$ and $\langle {}^{12}{\rm C}/{}^{14}{\rm N}\rangle_{\rm RC} = 1.40$, excluding the two evolved stars with $\log g < 2.1$ dex, which places them on the upper RGB or possibly in an early-AGB phase of evolution.

Figure 8 also highlights differences in the C and N abundance variations predicted from mixing models when compared to those abundances derived in this study. In the left panels of Figure 8 (a) and (b), we show the [C/N] ratio as a function of $T_{\rm eff}$ and $\log g$, respectively, and we note that the overall observational results follow the model predictions, although the observed [C/N] values are systematically lower. Such a difference can be a consequence of an overestimated nitrogen abundance in our analysis (as pointed out by Bertelli Motta et al. 2017 using ASPCAP data), due to a subestimated $\log g$. In the right panels of Figure 8, we present the [C/H] (panel (c)) and [N/H] (panel (d)) abundances as a function of $\log g$. For nitrogen, the abundances are in agreement with the models; however, the observational carbon abundances differ from the models by ~-0.15 dex. We conclude that the abundance variations observed for ^{12}C and ^{14}N in the subgiant and red giant stars can be explained well by FDU mixing models. The mixing models here (as well as from Lagarde et al. 2012) predict changes for the other elemental abundances to be smaller than 0.01 dex as the star evolves. Therefore, mixing models cannot explain their abundance variations.

6.3. Atomic Diffusion

Atomic diffusion is a likely explanation for most of the observed abundance variations across the H-R diagram in M67, thus adding members of this old open cluster to those stars in which diffusion has been observed. Evidence of diffusion in the Sun is found both in its surface helium abundance, which is lower than the initial value, and in the solar sound speed profile being best fit by models that include diffusion (Bahcall et al. 1995; Chaboyer et al. 1995a). Lithium abundances settle at a rate similar to He, and the flatness of the Spite Li plateau is likely set by diffusion (Chaboyer et al. 1992). The diffusion signature can be altered or erased by mixing, for example, mixing driven by rotation and dredge-up (see Section 6.2), thus complicating the detection and interpretation of diffusion patterns. Such mixing processes are likely at work in the Sun, which has a smoother composition profile than that predicted by diffusion alone, with the magnitude of diffusion being overestimated by about 25%. This is also confirmed by looking at A-type stars: if they rotate fast enough, they are not chemically peculiar (Michaud 1970, see also Michaud et al. 2015). The interplay between diffusion creating abundance signatures that various mixing processes can then modify means that there are not necessarily firm theoretical predictions about the amplitude of the diffusion signature and its mass or metallicity dependence. Reasonably well-motivated trends can be expected, though, and Chaboyer et al. (1995b, 1995c), Choi et al. (2016), Dotter (2016), and Dotter et al. (2017) have approximated limits on how efficient diffusion can be in thin surface convective zones.

A few previous studies have probed atomic diffusion in cluster stars, with most of them focused on low-metallicity globular clusters: Korn et al. (2007), Lind et al. (2008), and Nordlander et al. (2012). The latter analyzed stars belonging to the globular cluster NGC 6397, with a metallicity [Fe/H] $= -2.00$ and age 13.5 Gyr, with their sample containing stars from the turnoff point (TOP) up to the RGB. The abundances of Li, Mg, Ca, Ti, Cr, and Fe in those studies were derived from high-resolution optical spectroscopy, and they found that changes in the stellar abundances for different evolutionary phases are in good agreement with predictions from diffusion models from the literature; see Richard et al. (2002, 2005). In particular, Nordlander et al. (2012) found abundance differences of 0.06 and 0.18 dex between TOP and RGB stars in NGC 6397, with the largest difference for Mg, and which is a much smaller variation than we see in M67, for

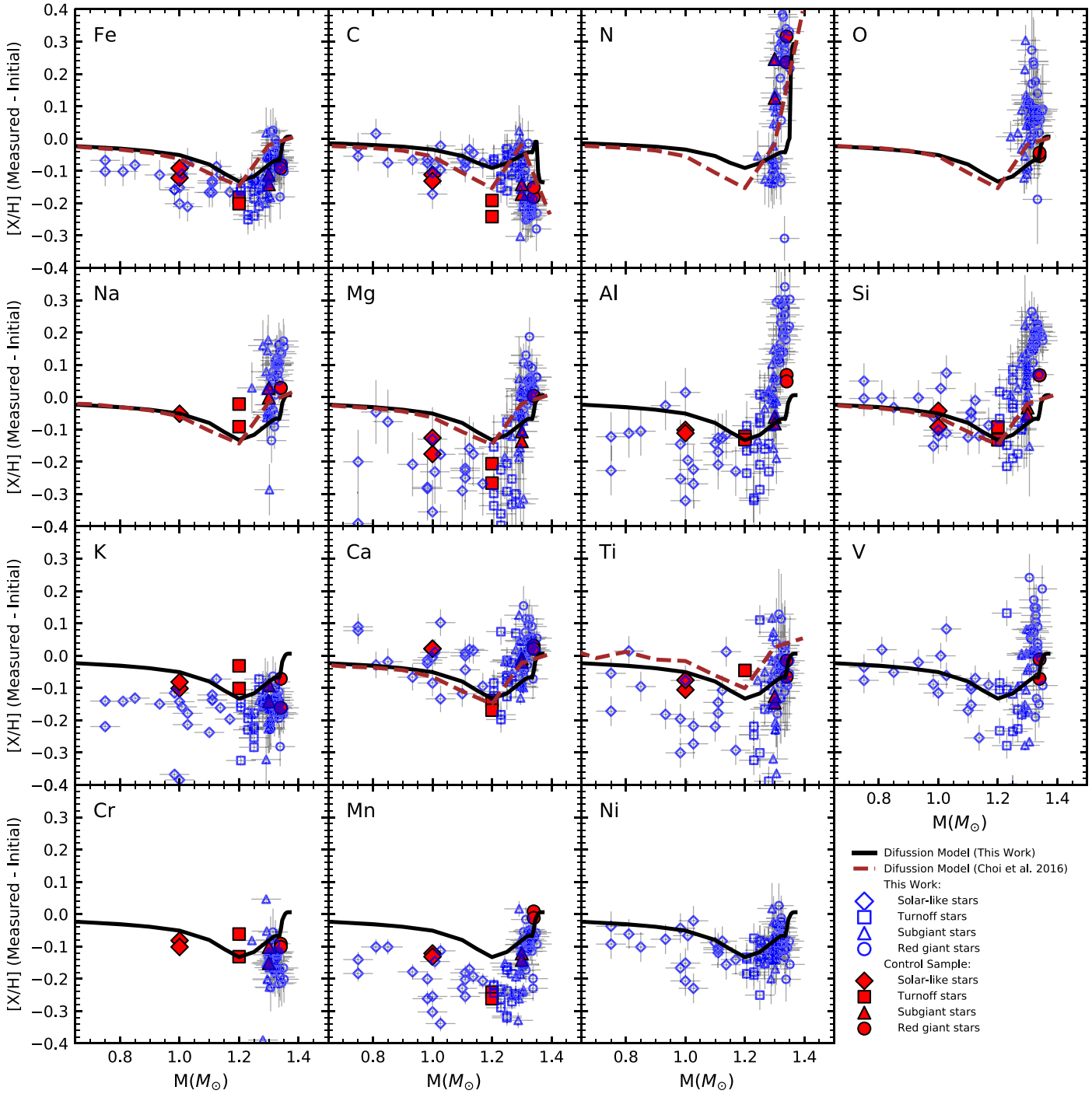

Figure 9. Diagram of the stellar mass as a function of Δ[X/H], where Δ[X/H] indicates the derived metallicity from the stellar photosphere minus the initial cluster composition. The black and brown lines show the atomic diffusion models from this work and MIST, respectively. All symbols follow the same notation as Figure 5.

example for Mg or Al. Of course, the chemical abundance of NGC 6397 is rather distinct from that of M67.

Önehag et al. (2014) found some evidence of atomic diffusion operating in M67. This was later supported by the abundance results in Blanco-Cuaresma et al. (2015). As previously mentioned, abundance differences of up to ~0.20 dex between the turnoff and red giant stars were observed by Souto et al. (2018) for the elements O, Na, Mg, Al, Si, Ca, V, Mn, and Fe. A comparison of the results in Souto et al. (2018) with the diffusion patterns from the models by Choi et al. (2016) and Dotter et al. (2017) indicated good agreement. In addition, Bertelli Motta et al. (2018) found >0.15 dex abundance differences from main-sequence to red giant stars for the elements Al, Si, Mn, and Ni. Gao et al. (2018) found a good match between the abundance variations for Al and Si with diffusion models.

6.4. Atomic Diffusion in M67 Stars

We find significant abundance differences (up to ~0.50 dex) for most of the studied species between main-sequence, turnoff, subgiant, and red giant stars in M67. Using the K-S test

(Figure 4), we obtained clear evidence of abundance differences between stars in different evolutionary stages in M67. In addition, we showed (Section 4) that the abundances of stars belonging to the same evolutionary class are indistinguishable.

In Figure 9 we present the mass–Δ[X/H] ($[X/H]_{Current}$–$[X/H]_{Initial}$) diagram for the 12 studied elements. Similar diagrams with abundances as a function of surface gravity and effective temperature are presented in Figures 5 and 6. In all three figures, we show the atomic diffusion models computed in this work as solid black lines and the MIST models as brown dashed lines. The pristine Fe abundance in the models is assumed to be the mean Fe abundance for the red giants, which is used as the fiducial point (i.e., δ[Fe/H] = 0.00) for the initial cluster value. We note that all other abundance ratios are assumed to be solar, that is, [X/Fe] = 0.00. The abundance variations across the H-R diagram indicate that atomic diffusion is operating in most of the studied elements. The models for all of the elements display similar trends driven by atomic diffusion, except for C and N, which include mixing signatures.

The complex trend observed in the carbon abundances is a consequence of diffusion operating in the main-sequence and turnoff stars (smaller convective envelopes), and mixing at the first dredge-up being responsible for the carbon abundance variation in subgiant and red giant stars (Section 6.2; Figure 8). These results suggest that atomic diffusion dominates over mixing in the main-sequence and turnoff stars, while mixing processes control the abundance changes in subgiant and red giant stars.

The nitrogen abundance variation can be explained as a signature of first dredge-up (Section 6.2). For oxygen, the scattered abundance results for red giant and subgiant stars, combined with the lack of results for main-sequence and turnoff stars, impedes detection of signatures of diffusion. Due to the weakness of CN and OH molecular lines in the APOGEE spectra of main-sequence and turnoff stars, it is not possible to derive N and O abundances in such stars.

The comparison of the abundance patterns for all elements with the model predictions indicates an overall good match between the atomic diffusion models and the derived abundances across the H-R diagram. However, the derived abundances exhibit a more significant dip across the main-sequence—turnoff stars when compared to what is expected from the atomic diffusion models, in particular for Mg, Al, Ti, and Mn.

For Al, Mg, Si, and to a lesser degree V, the relative dip across the main-sequence—turnoff stars is more significant because the red giant abundances are higher than those predicted by the models. (The Na abundances of red giants are also higher than the models, but there are no abundances for turnoff and main-sequence stars.) On the one hand, for Ti and Mn, the dip is more considerable because the abundances of turnoff and main-sequence stars are lower. As discussed in Section 5 (Figure 7), non-LTE corrections for Mg and Si (as well as Fe) would reduce the abundance dip by a factor of $\sim$0.03 dex, while for Ti, the dip would be reduced by roughly 0.05 dex. The non-LTE corrections for Mn, on the other hand, would systematically change the red giant abundances and increase the abundance difference between turnoff and red giant stars by $\sim$0.14 dex, which would worsen the comparison with the models.

7. Summary

Given its combination of age and metallicity in addition to the numerous detailed studies in the literature, M67 remains a prime cluster to test for physical and chemical processes in stellar spectroscopy that are not yet well understood.

In this paper, we present individual abundances of 15 elements (C, N, O, Na, Mg, Al, Si, K, Ca, Ti, V, Cr, Mn, Fe, and Ni) derived from a 1D LTE analysis of 83 stars in M67. The abundances were obtained via χ^2 minimization of the high-resolution SDSS-IV/APOGEE spectra with the qASP-CAP code. The stellar sample is composed of stars in different evolutionary stages (19 main sequence, 15 turnoff, 20 subgiant, and 29 red giants) with the aim to quantify abundance trends across the different stellar evolutionary phases (Önehag et al. 2014; Bertelli Motta et al. 2018; Gao et al. 2018; Souto et al. 2018).

We obtain significant abundance differences (of up to 0.30–0.40 dex) as a function of stellar parameters ($T_{\rm eff}$, $\log g$, and mass) that map the different stellar evolutionary classes. Studying the abundance variations within the same stellar classes, we find a much lower scatter, of about $\sim$0.05–0.10 dex. Using the K-S test, it is found that the abundances within each stellar class are indistinguishable; while performing the test for the different classes, we obtain clear segregations for the red giant and turnoff stars in most of the elements analyzed.

We compiled non-LTE corrections for Fe, Mg, Al, Si, and Mn, finding them to be small for all elements ($<$0.10 dex), except for Mn, which had corrections between 0.15 and 0.30 dex in all stellar classes analyzed. With the use of non-LTE corrections to our derived abundances, we still observe clear abundance trends across the H-R diagram.

We found that mixing models explain well the abundance variations of C and N for subgiants and red giant stars. We see atomic diffusion operating in the C abundances in stars from the main-sequence–TOP. The atomic diffusion models computed in this work (as well as from the literature) predict reasonably well the remaining abundance patterns for the stars at different evolutionary stages studied in this work, and therefore we conclude that atomic diffusion operates in M67 more efficiently in the turnoff stars and in most of the elements (C, Mg, Al, Si, K, Ca, Ti, V, Mn, Fe, and Ni) analyzed in this work.

We thank the anonymous referee for useful comments that helped improve the paper. D.S. thanks Pascal Petit for the cordial hosting at CNRS-Toulouse, where part of this project was developed. K.C. and V.S. acknowledge that their work here is supported, in part, by the National Aeronautics and Space Administration under Grant 16-XRP16_2-0004, issued through the Astrophysics Division of the Science Mission Directorate. D.A.G.H. and O.Z. acknowledge support from the State Research Agency (AEI) of the Spanish Ministry of Science, Innovation and Universities (MCIU) and the European Regional Development Fund (FEDER) under grant AYA2017-88254-P. H.J. acknowledges support from the Crafoord Foundation, Stiftelsen Olle Engkvist Byggmästare, and Ruth och Nils-Erik Stenbäcks stiftelse.

Funding for the Sloan Digital Sky Survey IV has been provided by the Alfred P. Sloan Foundation, the U.S. Department of Energy Office of Science, and the Participating Institutions. SDSS-IV acknowledges support and resources

from the Center for High-Performance Computing at the University of Utah. The SDSS website is www.sdss.org.

SDSS-IV is managed by the Astrophysical Research consortium for the Participating Institutions of the SDSS Collaboration including the Brazilian Participation Group, the Carnegie Institution for Science, Carnegie Mellon University, the Chilean Participation Group, the French Participation Group, Harvard-Smithsonian Center for Astrophysics, Instituto de Astrofísica de Canarias, The Johns Hopkins University, Kavli Institute for the Physics and Mathematics of the Universe (IPMU)/University of Tokyo, Lawrence Berkeley National Laboratory, Leibniz Institut für Astrophysik Potsdam (AIP), Max-Planck-Institut für Astronomie (MPIA Heidelberg), Max-Planck-Institut für Astrophysik (MPA Garching), Max-Planck-Institut für Extraterrestrische Physik (MPE), National Astronomical Observatory of China, New Mexico State University, New York University, University of Notre Dame, Observatório Nacional/MCTI, The Ohio State University, Pennsylvania State University, Shanghai Astronomical Observatory, United Kingdom Participation Group, Universidad Nacional Autónoma de México, University of Arizona, University of Colorado Boulder, University of Oxford, University of Portsmouth, University of Utah, University of Virginia, University of Washington, University of Wisconsin, Vanderbilt University, and Yale University.

ORCID iDs

Diogo Souto https://orcid.org/0000-0002-7883-5425
C. Allende Prieto https://orcid.org/0000-0002-0084-572X
Marc Pinsonneault https://orcid.org/0000-0002-7549-7766
Jo Bovy https://orcid.org/0000-0001-6855-442X
Jon Holtzman https://orcid.org/0000-0002-9771-9622
J. A. Johnson https://orcid.org/0000-0001-7258-1834
Henrik Jönsson https://orcid.org/0000-0002-4912-8609
Steve R. Majewski https://orcid.org/0000-0003-2025-3147
Matthew Shetrone https://orcid.org/0000-0003-0509-2656
Kaike Pan https://orcid.org/0000-0002-2835-2556

References

Abolfathi, B., Aguado, D. S., Aguilar, G., et al. 2018, ApJS, 235, 42
Allende Prieto, C., Beers, T. C., Wilhelm, R., et al. 2006, ApJ, 636, 804
Aller, L. H., & Chapman, S. 1960, ApJ, 132, 461
Alvarez, R., & Plez, B. 1998, A&A, 330, 1109
Amarsi, A. M., & Asplund, M. 2017, MNRAS, 464, 264
Amarsi, A. M., Asplund, M., Collet, R., & Leenaarts, J. 2016, MNRAS, 455, 3735
Asplund, M. 2005, ARA&A, 43, 481
Asplund, M., Grevesse, N., Sauval, A. J., & Scott, P. 2009, ARA&A, 47, 481
Bahcall, J. N., Pinsonneault, M. H., & Basu, S. 2001, ApJ, 555, 990
Bahcall, J. N., Pinsonneault, M. H., & Wasserburg, G. J. 1995, RvMP, 67, 781
Bailer-Jones, C. A. L., Rybizki, J., Fouesneau, M., Mantelet, G., & Andrae, R. 2018, AJ, 156, 58
Balachandran, S. 1990, ApJ, 354, 310
Balachandran, S. 1995, ApJ, 446, 203
Bellini, A., Bedin, L. R., Pichardo, B., et al. 2010, A&A, 513, A51
Benjamini, Y., & Hochberg, Y. 1995, Journal of the Royal Statistical Society, 57, 289
Bergemann, M., Collet, R., Amarsi, A. M., et al. 2017, ApJ, 847, 15
Bergemann, M., & Gehren, T. 2008, A&A, 492, 823
Bergemann, M., Kudritzki, R.-P., Gazak, Z., Davies, B., & Plez, B. 2015, ApJ, 804, 113
Bergemann, M., Kudritzki, R.-P., Plez, B., et al. 2012a, ApJ, 751, 156
Bergemann, M., Kudritzki, R.-P., Würl, M., et al. 2013, ApJ, 764, 115
Bergemann, M., Lind, K., Collet, R., Magic, Z., & Asplund, M. 2012b, MNRAS, 427, 27
Bertelli Motta, C., Pasquali, A., Richer, J., et al. 2018, MNRAS, 478, 425
Bertelli Motta, C., Salaris, M., Pasquali, A., & Grebel, E. K. 2017, MNRAS, 466, 2161
Bertran de Lis, S., Allende Prieto, C., Majewski, S. R., et al. 2016, A&A, 590, A74
Blanco-Cuaresma, S., Soubiran, C., Heiter, U., et al. 2015, A&A, 577, A47
Blanton, M. R., Bershady, M. A., Abolfathi, B., et al. 2017, AJ, 154, 28
Bovy, J. 2016, ApJ, 817, 49
Bressan, A., Marigo, P., Girardi, L., et al. 2012, MNRAS, 427, 127
Caffau, E., Ludwig, H.-G., Steffen, M., Freytag, B., & Bonifacio, P. 2011, SoPh, 268, 255
Caffau, E., Maiorca, E., Bonifacio, P., et al. 2009, A&A, 498, 877
Canto Martins, B. L., Lèbre, A., Palacios, A., et al. 2011, A&A, 527, A94
Castelli, F., & Kurucz, R. L. 2004, arXiv:astro-ph/0405087
Chaboyer, B., Deliyannis, C. P., Demarque, P., Pinsonneault, M. H., & Sarajedini, A. 1992, ApJ, 388, 372
Chaboyer, B., Demarque, P., Guenther, D. B., & Pinsonneault, M. H. 1995a, ApJ, 446, 435
Chaboyer, B., Demarque, P., & Pinsonneault, M. H. 1995b, ApJ, 441, 865
Chaboyer, B., Demarque, P., & Pinsonneault, M. H. 1995c, ApJ, 441, 876
Chapman, S. 1917a, MNRAS, 77, 540
Chapman, S. 1917b, MNRAS, 77, 539
Charbonnel, C., & Zahn, J.-P. 2007, A&A, 467, L15
Choi, J., Dotter, A., Conroy, C., et al. 2016, ApJ, 823, 102
Cohen, J. G. 1980, ApJ, 241, 981
Cunha, K., Smith, V. V., Hasselquist, S., et al. 2017, ApJ, 844, 145
Cunha, K., Smith, V. V., Johnson, J. A., et al. 2015, ApJL, 798, L41
da Silva, L., Torres, C. A. O., de La Reza, R., et al. 2009, A&A, 508, 833
Delahaye, F., & Pinsonneault, M. H. 2006, ApJ, 649, 529
Delgado Mena, E., Israelian, G., González Hernández, J. I., et al. 2014, A&A, 562, A92
De Silva, G. M., Freeman, K. C., Asplund, M., et al. 2007, AJ, 133, 1161
De Silva, G. M., Freeman, K. C., Bland-Hawthorn, J., et al. 2015, MNRAS, 449, 2604
De Silva, G. M., Sneden, C., Paulson, D. B., et al. 2006, AJ, 131, 455
Dotter, A. 2016, ApJS, 222, 8
Dotter, A., Conroy, C., Cargile, P., & Asplund, M. 2017, ApJ, 840, 99
Eggleton, P. P., Dearborn, D. S. P., & Lattanzio, J. C. 2006, Sci, 314, 1580
Eisenstein, D. J., Weinberg, D. H., Agol, E., et al. 2011, AJ, 142, 72
El-Badry, K., Ting, Y.-S., Rix, H.-W., et al. 2018, MNRAS, 476, 528
Foy, R., & Proust, D. 1981, A&A, 99, 221
Gaia Collaboration, Brown, A. G. A., Vallenari, A., et al. 2018, A&A, 616, A1
Gao, X., Lind, K., Amarsi, A. M., et al. 2018, MNRAS, 481, 2666
García Pérez, A. E., Allende Prieto, C., Holtzman, J. A., et al. 2016, AJ, 151, 144
Geller, A. M., Latham, D. W., & Mathieu, R. D. 2015, AJ, 150, 97
Gilmore, G., Randich, S., Asplund, M., et al. 2012, Msngr, 147, 25
González-Hernández, J. I., & Bonifacio, P. 2009, A&A, 497, 497
Gunn, J. E., Siegmund, W. A., Mannery, E. J., et al. 2006, AJ, 131, 2332
Hasselquist, S., Shetrone, M., Cunha, K., et al. 2016, ApJ, 833, 81
Holtzman, J. A., Hasselquist, S., Shetrone, M., et al. 2018, AJ, 156, 125
Holtzman, J. A., Shetrone, M., Johnson, J. A., et al. 2015, AJ, 150, 148
Iben, I., Jr. 1965, ApJ, 142, 1447
Jacobson, H. R., Pilachowski, C. A., & Friel, E. D. 2011, AJ, 142, 59
Karakas, A. I., & Lattanzio, J. C. 2014, PASA, 31, e030
King, J. R., Krishnamurthi, A., & Pinsonneault, M. H. 2000, AJ, 119, 859
Korn, A. J., Grundahl, F., Richard, O., et al. 2007, ApJ, 671, 402
Lagarde, N., Decressin, T., Charbonnel, C., et al. 2012, A&A, 543, A108
Lind, K., Korn, A. J., Barklem, P. S., & Grundahl, F. 2008, A&A, 490, 777
Liu, F., Asplund, M., Yong, D., et al. 2016, MNRAS, 463, 696
Majewski, S. R., Schiavon, R. P., Frinchaboy, P. M., et al. 2017, AJ, 154, 94
Martig, M., Fouesneau, M., Rix, H.-W., et al. 2016, MNRAS, 456, 3655
Masseron, T., & Gilmore, G. 2015, MNRAS, 453, 1855
Masseron, T., Lagarde, N., Miglio, A., Elsworth, Y., & Gilmore, G. 2017, MNRAS, 464, 3021
Mészáros, S., Allende Prieto, C., Edvardsson, B., et al. 2012, AJ, 144, 120
Mészáros, S., Holtzman, J., García Pérez, A. E., et al. 2013, AJ, 146, 133
Michaud, G. 1970, ApJ, 160, 641
Michaud, G. 1980, AJ, 85, 589
Michaud, G., Alecian, G., & Richer, J. 2015, Atomic Diffusion in Stars (Cham: Springer International)
Michaud, G., Charland, Y., Vauclair, S., & Vauclair, G. 1976, ApJ, 210, 447
Michaud, G., Richard, O., Richer, J., & VandenBerg, D. A. 2004, ApJ, 606, 452
Ness, M., Hogg, D. W., Rix, H.-W., et al. 2016, ApJ, 823, 114

Nidever, D. L., Holtzman, J. A., Allende Prieto, C., et al. 2015, AJ, 150, 173
Nordlander, T., Korn, A. J., Richard, O., & Lind, K. 2012, ApJ, 753, 48
Önehag, A., Gustafsson, B., & Korn, A. 2014, A&A, 562, A102
Pancino, E., Carrera, R., Rossetti, E., & Gallart, C. 2010, A&A, 511, A56
Plez, B. 2012, Turbospectrum: Code for Spectral Synthesis, Astrophysics Source Code Library, ascl:1205.004
Price-Jones, N., & Bovy, J. 2018, MNRAS, 475, 1410
Prša, A., Harmanec, P., Torres, G., et al. 2016, AJ, 152, 41
Randich, S., Gilmore, G. & Gaia-ESO Consortium 2013, Msngr, 154, 47
Reddy, A. B. S., Giridhar, S., & Lambert, D. L. 2012, MNRAS, 419, 1350
Richard, O., Michaud, G., & Richer, J. 2002, ApJ, 580, 1100
Richard, O., Michaud, G., & Richer, J. 2005, ApJ, 619, 538
Sarajedini, A., Mancone, C. L., Lauer, T. R., et al. 2009, AJ, 138, 184
Shetrone, M., Bizyaev, D., Lawler, J. E., et al. 2015, ApJS, 221, 24
Skrutskie, M. F., Cutri, R. M., Stiening, R., et al. 2006, AJ, 131, 1163
Smith, V. V., Cunha, K., Shetrone, M. D., et al. 2013, ApJ, 765, 16
Souto, D., Cunha, K., Smith, V., et al. 2016, ApJ, 830, 35
Souto, D., Cunha, K., Smith, V. V., et al. 2018, ApJ, 857, 14
Tautvaišiene, G., Edvardsson, B., Tuominen, I., & Ilyin, I. 2000, A&A, 360, 499
Taylor, B. J. 2007, AJ, 134, 934
Vauclair, G., Vauclair, S., & Michaud, G. 1978, ApJ, 223, 920
Vauclair, S., & Vauclair, G. 1982, ARA&A, 20, 37
Wilson, J. C., Hearty, F., Skrutskie, M. F., et al. 2010, Proc. SPIE, 7735, 77351C
Yadav, R. K. S., Bedin, L. R., Piotto, G., et al. 2008, A&A, 484, 609
Yakut, K., Zima, W., Kalomeni, B., et al. 2009, A&A, 503, 165
Zacharias, N., Finch, C., Subasavage, J., et al. 2015, AJ, 150, 101
Zamora, O., García-Hernández, D. A., Allende Prieto, C., et al. 2015, AJ, 149, 181
Zasowski, G., Johnson, J. A., Frinchaboy, P. M., et al. 2013, AJ, 146, 81
Zhang, J., Shi, J., Pan, K., Allende Prieto, C., & Liu, C. 2016, ApJ, 833, 137
Zhang, J., Shi, J., Pan, K., Allende Prieto, C., & Liu, C. 2017, ApJ, 835, 90